Coherent Control of Single $^{40}Ca^{+}$ Qubits in a Linear Paul Trap

A Thesis submitted to
Indian Institute of Science Education and Research Pune
in partial fulfilment of the requirements for the
BS-MS Dual Degree Programme

by

Sharan K

Indian Institute of Science Education and Research Pune
Dr. Homi Bhabha Road,
Pashan, Pune 411008, INDIA.

May 2026

Supervisor: Prof. Umakant D. Rapol

Certificate

This is to certify that this dissertation entitled **"Coherent Control of Single $^{40}Ca^{+}$ Qubits in a Linear Paul Trap"** towards the partial fulfilment of the BS-MS dual degree programme at the Indian Institute of Science Education and Research, Pune represents study/work carried out by **Sharan K** at Indian Institute of Science Education and Research Pune under the supervision of **Prof. Umakant D. Rapol, Professor, Department of Physics** during the academic year 2025-2026.

19/05/2026

Sharan K
(Student)

Prof. Umakant D. Rapol
(Supervisor)

Dedicated to my parents,
S. Kumar and P. Uma Maheswari

Declaration

I hereby declare that the matter embodied in the report entitled **"Coherent Control of Single $^{40}Ca^{+}$ Qubits in a Linear Paul Trap"** are the results of the work carried out by me at the Department of Physics, Indian Institute of Science Education and Research Pune, under the supervision of **Prof. Umakant D. Rapol** and the same has not been submitted elsewhere for any other degree.

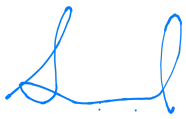

19/05/2026

Sharan K
(Student)

Acknowledgements

First of all, I express immense gratitude to my supervisor, Prof. Umakant D. Rapol for giving me an opportunity to work in a state-of-the-art Atomic Physics and Optics Lab as my first exposure to experimental physics. His relentless passion and drive for research definitely pushed me to work harder, and gave me a fresh perspective on physics.

Words are not enough to thank Rayees A.S. and Shuvarati Roy for their constant mentoring and guidance from my day one in the lab. This thesis would not have been possible if not for such supportive seniors helping me and correcting my mistakes. Special mention goes to Ganesh and Atharva for fully developing the *ARTIQ* control environment, forming the backbone of this project. I would also like to thank Trivijay, Kshitija and Niranjan for their valuable discussions and timely contributions to the Ion Trap project this thesis is a part of.

I thank all my friends, both on and off campus who supported me through the highs and lows in my thesis year, for being the safe space I can always fall back to. Lastly I thank my parents, for being there for me through every decision, hardship, joy and sorrow, for always believing in me.

I declare that the use of Generative AI in this thesis did not extend beyond what is described in Section 4.6.1 of the 'Guidelines for Generative AI usage at IISER Pune', and accordingly, no attribution is required.

Abstract

Quantum computation has been a steadily advancing field of research with potential extensive applications in academia as well as industry. Trapped-ion systems are one of the frontrunners in the race for physical platforms for realizing the true potential of quantum computers.

This thesis describes the design, characterization and coherent control of a single $^{40}Ca^{+}$ ion in a linear Paul trap. We demonstrate the ability to implement Doppler cooling to reduce the motional energy of ions, trap and image single and multiple ions with the cooling transition fluorescence and perform pulsed spectroscopy on the quadrupole transition using electron shelving detection technique. We characterize the spectrum of the qubit transition and identify the carrier and motional sidebands by analyzing the shift of the peaks with an applied magnetic field. We also show coherent control over the internal states of the ion by demonstrating Rabi oscillations on the qubit transition.

The results presented in this thesis lay the groundwork for future experiments involving multi-qubit gates and entanglement generation in trapped-ion systems, which are essential for realizing the full potential of quantum computation.

Contents

List of Figures

List of Tables

Chapter 1

Introduction

Quantum mechanics has fundamentally reshaped our understanding of nature at microscopic scales. Developed in the early twentieth century to explain phenomena such as the photoelectric effect and UV catastrophe that could not be described by classical physics, it introduced wave-particle duality, quantization of energy levels, and non-deterministic nature of measurement. These ideas were so radical even a physics giant like Einstein was critical about it, famously remarking that he could not accept a theory in which "God plays dice" [1]. Despite early skepticism, quantum mechanics withstood the test of time and established itself as one of the leading theories to explain macroscopic objects to subatomic particles.

In recent decades, the scope of quantum mechanics has expanded beyond explaining natural phenomena to enabling new forms of technology. One of the most exciting developments in this direction is the field of *quantum computation*. The basic idea is that the principles of quantum mechanics themselves can be used to process and manipulate information. Simulation of quantum systems in classical computers is computationally intensive and the resources required grow exponentially with the size of the system. Quantum computers, on the other hand, can efficiently simulate quantum systems. As famously quoted by Richard Feynman "Nature isn't classical, dammit, and if you want to make a simulation of nature, you'd better make it quantum mechanical." [2], quantum computers in theory outperform classical computers. Overcoming the physical challenges of building a quantum computer is a whole another ball game.

Quantum computation encompasses the usage of quantum bits or widely known as "qubits" for encoding information about the system. This is a quantum mechanical analogue of bits (0 and 1) in classical computers, where two different *states* of the quantum system act as the "0" and "1" states. What distinguishes qubits from classical bits, is the ability of the system to exist in a *superpostion* of the two states ($|0\rangle$ and $|1\rangle$). Like any other quantum system, it's dynamics is governed by a unitary transform, namely, the Hamiltonian acting on the Hilbert space

spanned by $|0\rangle$ and $|1\rangle$. This opens the door to a wide range of possibilities, but also practical complications. The theoretical potential of quantum computation became widely recognized after the discovery of several quantum algorithms demonstrating significant speedups over classical methods. One notable example is Shor's algorithm [3] for factorization of large integers which are used in many cryptographic protocols. Another important development was Grover's search algorithm [4], which provides a quadratic speedup for searching unsorted databases.

1.1 Physical Platforms for Quantum Computation

These developments motivated the search for physical systems capable of implementing qubits with high precision and reliability. However, realizing a practical quantum computer poses substantial experimental challenges. Quantum states are extremely sensitive to environmental disturbances, and interactions with external degrees of freedom can lead to decoherence, which destroys the quantum information stored in the system. Consequently, a successful quantum computing platform must allow precise control over quantum states while simultaneously maintaining long coherence times.

To address these requirements, David DiVincenzo formulated a set of criteria [5], that any physical system intended for quantum computation should satisfy.

1. A **scalable** physical system with well characterized qubits
2. The ability to **initialize** the state of the qubits to a simple **fiducial** state
3. **Relevant coherence times** much longer than the gate operation time
4. A **universal** set of quantum gates
5. A qubit-specific **measurement** capability

Several physical systems have been explored as potential candidates for implementing quantum computers. Among the most prominent approaches are superconducting circuits [6], photonic systems [7], neutral atoms [8], semiconductor qubits [9], and trapped ions [10]. Each of these platforms has its own advantages and technological challenges.

Despite these promising alternatives, trapped-ion systems remain one of the most mature and experimentally successful platforms for quantum information processing. Trapped ions exhibit exceptionally long coherence times, extremely high gate fidelities, and precise individual

qubit control. These features arise from the fact that ions are naturally abundant atomic systems with well-defined and highly reproducible energy levels that are largely immune to many sources of environmental noise.

Recent experimental advances demonstrate the rapid progress of trapped-ion technology. Modern systems have achieved multi-qubit entanglement involving dozens of ions and high-fidelity quantum logic gates, while commercial quantum computing platforms based on trapped ions are now being developed by companies such as *IonQ* [10] and *Quantinuum* [11]. Experiments have also demonstrated modular architectures capable of scaling trapped-ion processors to larger numbers of qubits.

1.2 Ion Trapping and the Paul Trap

The ability to trap and manipulate charged particles using electromagnetic fields forms the experimental foundation of trapped-ion quantum computing. The earliest foundations of confinement of charged particles were laid in the 1930s by Frans Michel Penning, who developed a way to increase the path length of electrons in a gas discharge tube using static electric and magnetic fields [12].

Wolfgang Paul carried forward this field by realizing a quadrupole mass filter [13] which takes magnetic field out of the picture and creates stable trajectories for charged particles of a given charge-mass ratio. Different geometries of the mass filter were subsequently developed to even confine charged particles. Subsequent work expanded the design and capabilities of ion traps. Fischer demonstrated the stabilization of charged particles in three-dimensional quadrupole fields [14], while Wuerker and collaborators developed improved trapping configurations capable of stable confinement [15]. Combined efforts in this line of work led to the invention of the radio-frequency ion trap, commonly known as the Paul trap.

In a Paul trap, ions are confined using a time-varying quadrupole electric field generated by applying radio-frequency voltages to specially shaped electrodes. Although a purely static electric field cannot confine a charged particle in 3D space due to Earnshaw's theorem, the use of rapidly oscillating fields produces a time-averaged effective potential that provides stable confinement. This effective trapping potential can often be approximated as a harmonic pseudopotential in which ions undergo small oscillations about an equilibrium position.

Paul traps were primarily used then, for ion mass spectrometry and collision measurements. The advent of laser cooling techniques [16] in the 1970s and 1980s enabled the cooling of trapped ions to temperatures near millikelvins. This opened the door to the vast field of precision spectroscopy and quantum control of trapped ions. A major experimental milestone

occurred in 1980 when a single barium ion was successfully trapped and observed using laser fluorescence [17]. This demonstration established the feasibility of manipulating individual atomic ions and paved the way for later developments in quantum information research.

1.3 Quantum Computation with Trapped Ions

The connection between ion trapping and quantum computation was established when Cirac and Zoller proposed a method to implement quantum gates using ion trap systems [18]. In this scheme, the electronic energy levels of the ions are used as qubits, while the collective vibrational modes of the ion chain act as a quantum bus that mediates interactions between qubits. This allows for all-to-all connectivity and high-fidelity gate operations.

Paul traps satisfy the DiVincenzo criteria for quantum computation to a high degree. A variety of ion species have been used in trapped-ion experiments, including barium, ytterbium, strontium, and calcium. Among these, the singly ionized calcium atom ($^{40}Ca^{+}$) is widely used due to its convenient energy level structure and accessible optical transitions. Modular architectures have been proposed and achieved **scaling** upto 32-qubit entanglement [11]. Methods such as sideband cooling can be used to **initialize** the qubit in its motional ground state. Theoretical limit of the **coherence time** of the optical qubit is the excited state lifetime, which in this case is $\sim$ 1s of the $D_{5/2}$ state of a $^{40}Ca^{+}$ ion. **Universal set of gates** can realized by addressing the $S_{1/2} \rightarrow D_{5/2}$ transition and driving the motional sidebands to entangle two qubits [19, 20]. Electron-shelving based fluorescence detection allows for near-zero **state measurement** error. The first experimental demonstration of a two-qubit gate using trapped ions was achieved by Monroe and colleagues in the same year [21], marking a significant milestone in the field.

1.4 Objectives of this Thesis

The work presented in this thesis focuses on the experimental realization of coherent control over a single qubit encoded in a trapped $^{40}Ca^{+}$ ion confined in a linear Paul trap. Achieving precise coherent control of single qubits is a fundamental requirement for implementing quantum gate operations and forms the basis of scalable quantum information processing.

In this experiment, the qubit transition of the calcium ion is addressed using a narrow linewidth 729 nm laser. By applying laser pulses of controlled duration, it is possible to have coherent control over the qubit. These oscillations correspond to coherent rotations of a vector on the Bloch sphere (see fig. 2.1) and provide a direct demonstration of single-qubit gate operations.

The primary goals of this thesis are therefore:

- To demonstrate stable trapping and imaging of $^{40}Ca^{+}$ ions in a linear Paul trap.
- To perform spectroscopy of the $S_{1/2} \leftrightarrow D_{5/2}$ quadrupole transition using a stabilized 729 nm laser.
- To observe Rabi oscillations between the qubit states and determine the corresponding Rabi frequency and doppler cooling efficiency.

The scope of this thesis is limited to the coherent control of a single ion in a linear Paul trap and the characterization of the experimental apparatus required for such control. While large-scale quantum computation requires multi-qubit entanglement and single-ion addressing, the techniques developed here form the fundamental building blocks for such future experiments.

1.5 Thesis Outline

The organization of this thesis is given below:

Chapter 2 presents the theoretical background required for understanding the experiments described in this work. This includes an introduction to quantum computation, the Bloch sphere representation of qubit states, and the principles of quantum gate operations. The chapter also discusses the principles behind ion traps and it's interaction with light.

Chapter 3 describes the experimental setup, including the design of the linear Paul trap, the vacuum system, laser sources, optical layout, and control electronics. Methods used for ion loading, Doppler cooling, and state detection are also discussed.

Chapter 4 presents the experimental results obtained in this work, including the imaging of trapped ions, spectroscopy of the quadrupole transition, and the measurement of Rabi oscillations demonstrating coherent control of the qubit.

Chapter 5 concludes the thesis with a summary of the main findings and a discussion of future directions for research in this line of work.

Chapter 2

Theoretical Foundations

This chapter briefly discusses the theoretical framework on which this thesis is based on. First, a basic introduction to quantum computation is given where its foundations are explained, followed by a section on the fundamental working principle of linear paul traps and sources of instabilities. Then, we address our system and see how exactly quantum gate protocols are achieved on $^{40}Ca^{+}$ ions in Paul traps.

2.1 Quantum Computation

In classical computers, encoding of information is done as 0s and 1s. Physically, they are attributed to different voltage levels of transistors. A quantum bit, popularly known as a *qubit* is represented by two discrete quantum states of a system, given by $|0\rangle$ and $|1\rangle$. A qubit can exist in a superposition of these states like:

$$|\psi\rangle = \mathrm{a}\,|0\rangle + \mathrm{b}\,|1\rangle$$

where $\mathrm{a}, \mathrm{b} \in \mathbb{C}$ and satisfy the normalization condition $|\mathrm{a}|^2 + |\mathrm{b}|^2 = 1$. The squared modulus of coefficients a and b give us the probability of the qubit being present in $|0\rangle$ and $|1\rangle$ respectively, upon measurement. This interpretation is facilitated by the normalization condition. This section is primarily referenced from [22].

2.1.1 Bloch sphere

The Hilbert space spanned by $|0\rangle$ and $|1\rangle$ can be represented as a sphere in 3D, where each point on the sphere represents a possible state in the Hilbert space. This is called the *Bloch*

Sphere. This is possible because of the following representation of $|\psi\rangle$:

$$|\psi\rangle = e^{i\gamma}\left(\cos\frac{\theta}{2}|0\rangle + e^{i\phi}\sin\frac{\theta}{2}|1\rangle\right) \tag{2.1}$$

where θ and ϕ uniquely determine every possible state in the Hilbert space. These parameters can be thought of as polar and azimuthal angles in the Bloch sphere as shown in fig. 2.1.

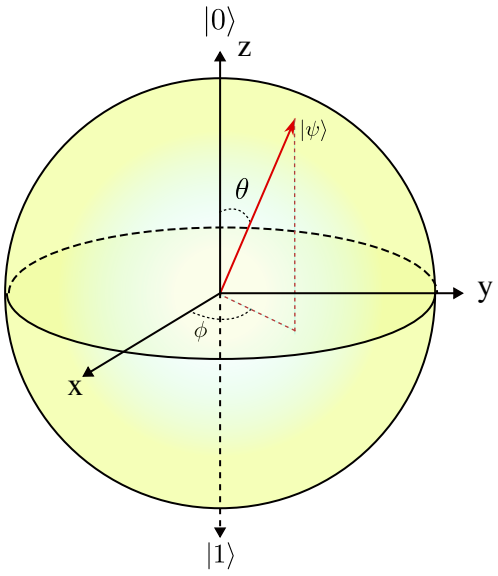

Figure 2.1: A qubit visualized in the Bloch sphere. The state $|\psi\rangle$ is completely characterized by the angles θ and ϕ, where the basis states $|0\rangle$ and $|1\rangle$ are at the north and south poles.

2.1.2 Quantum Gates

Classical logic gates are the building blocks of digital computation. The same way a complicated algorithm can be broken down into fundamental logic gates, there also exists *quantum gates* which process quantum information.

A general qubit state is a vector in the 2D complex vector space spanned by basis states $|0\rangle \equiv [1 \quad 0]^T$ and $|1\rangle \equiv [0 \quad 1]^T$:

$$|\psi\rangle = \alpha\begin{bmatrix}1\\0\end{bmatrix} + \beta\begin{bmatrix}0\\1\end{bmatrix}$$

Due to the nature of a qubit as we saw in section 2.1.1, we know that any operation or *gate* which transforms the state across the Bloch sphere surface has to be **linear** and **norm-preserving**. Thus, the matrix transformations on the vector must be unitary. Since $\alpha, \beta \in \mathbb{C}$, the space of linear transformations is an SU(2) group, assuming we ignore the global phase which may arise as $e^{i\gamma}$, which is removed by putting a constraint on the matrix trace. We know

that the Lie algebra of a matrix Lie group $(\mathrm{SU}(2))$ is a generator for the group itself [23].

The Lie algebra of $\mathrm{SU}(2)$ is spanned by the **Pauli spin matrices**.

$$\sigma_x = \begin{bmatrix} 0 & 1 \\ 1 & 0 \end{bmatrix}, \quad \sigma_y = \begin{bmatrix} 0 & -i \\ i & 0 \end{bmatrix}, \quad \sigma_z = \begin{bmatrix} 1 & 0 \\ 0 & -1 \end{bmatrix} \tag{2.2}$$

Any Lie group element can be written as a product of matrix exponential of its Lie algebra [23]. We write a general exponential matrix for $\mathrm{SU}(2)$ with the Pauli matrices as:

$$\mathrm{R}_n(\theta) = \exp\left\{-\frac{\theta}{2}\vec{\sigma}\cdot\vec{n}\right\} = \mathbb{I}\cdot\cos\left(\frac{\theta}{2}\right) - i\sin\left(\frac{\theta}{2}\right)(\vec{\sigma}\cdot\vec{\mathrm{n}}) \tag{2.3}$$

where $\vec{\sigma} \equiv [\sigma_x \quad \sigma_y \quad \sigma_z]^T$ is a Pauli vector and $\vec{\mathrm{n}} \equiv [n_x \quad n_y \quad n_z]^T$ is a unit vector on the bloch sphere. Now evaluating the matrices for each basis unit vector along x, y and z:

$$R_x(\theta) = \begin{bmatrix} \cos\frac{\theta}{2} & -i\sin\frac{\theta}{2} \\ -i\sin\frac{\theta}{2} & \cos\frac{\theta}{2} \end{bmatrix} \tag{2.4}$$

$$R_y(\theta) = \begin{bmatrix} \cos\frac{\theta}{2} & -\sin\frac{\theta}{2} \\ \sin\frac{\theta}{2} & \cos\frac{\theta}{2} \end{bmatrix} \tag{2.5}$$

$$R_z(\theta) = \begin{bmatrix} e^{-i\frac{\theta}{2}} & 0 \\ 0 & e^{i\frac{\theta}{2}} \end{bmatrix} \tag{2.6}$$

We can see that each of these matrices correspond to rotation matrices in 3D by an angle θ, about the three cartesian axes. Thus, any arbitrary unitary transform on a general qubit state, can be visualized as a rotation on the Bloch sphere.

A classical *NOT* gate acts on a logical bit and inverts it. Similarly we can have a *quantum NOT* gate as an action of $\mathrm{R}_x(\pi)$ on a qubit up to a global phase of $-i$. This applies to all π rotations and the X (NOT), Y, and Z (phase flip) gates are defined as $-i\mathrm{R}_x(\pi)$, $-i\mathrm{R}_y(\pi)$ and $-i\mathrm{R}_z(\pi)$ respectively. For example:

$$X|0\rangle = -iR_x(\pi)|0\rangle = -i\begin{bmatrix}\cos\frac{\pi}{2} & -i\sin\frac{\pi}{2}\\ -i\sin\frac{\pi}{2} & \cos\frac{\pi}{2}\end{bmatrix}\begin{bmatrix}1\\0\end{bmatrix}$$

$$= -\begin{bmatrix}0 & 1\\ 1 & 0\end{bmatrix}\begin{bmatrix}1\\0\end{bmatrix}$$

$$= -\begin{bmatrix}0\\1\end{bmatrix}$$

$$X|0\rangle = -|1\rangle$$

Similarly, rotations of $\pi/2$ puts a basis qubit in an equal superposition, like $\frac{1}{\sqrt{2}}(|0\rangle + |1\rangle)$. Experimental realization of such operations will be discussed in section 2.4.

2.2 The Linear Paul Trap

Earnshaw theorem states that "a collection of point charges cannot be maintained in a stable stationary equilibrium configuration in three dimensions solely by the electrostatic interaction of the charges.". This follows from the Laplace equation which states that the potential in a charge-free region must satisfy $\Delta\Phi = 0$, whose solutions cannot have local extrema. Thus a need for time-varying potentials for trapping ions arose and was initially realized by Wolfgang Paul [13]. A linear Paul trap creates a harmonic pseudopotential in 3D that traps charged particles in a specific range of charge-mass ratio. The radial field is generated by a time-varying RF potential and axial field by DC voltages. The following discussions on the principles of ion trap are primarily referenced from [24, 25].

2.2.1 2D Quadrupole Field

Take for instance, a quadrupole potential of the form:

$$\Phi(x,y) = \frac{\Phi_0}{2r_0^2}[\alpha_x x^2 + \alpha_y y^2] \tag{2.7}$$

The Laplace equation demands that $\Delta\Phi = 0$ for an equilibrium state, which gives the relation for the coefficients as $\alpha_x = -\alpha_y$ and without loss of generality, we take $\alpha_x = 1$.

$$\Phi(x,y) = \frac{\Phi_0}{2r_0^2}[x^2 - y^2] \tag{2.8}$$

This kind of potential (see fig. 2.2a) is created by four equidistant hyperbolic electrodes, with voltages $\pm\Phi_0/2$ applied across diagonally opposite electrodes,

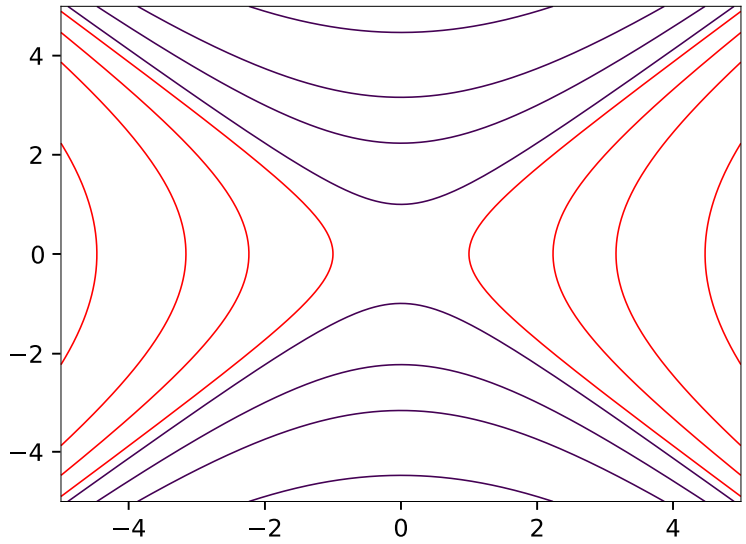

(a) Equipotential contour lines

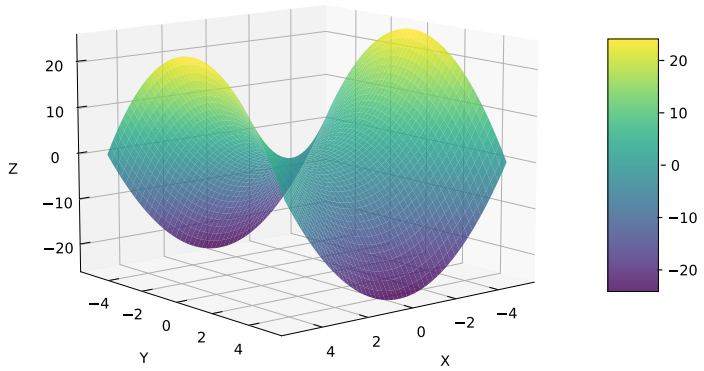

(b) 3D plot of the quadrupole potential

Figure 2.2: Visualization near the axis of the hyperbolic electrodes in the $x-y$ plane

where r_0 is the perpendicular distance from the ions to the RF blades. In this thesis, we

ground one pair of electrodes (see fig. 2.3) and apply the full voltage Φ_0 to the other pair which is equivalent.

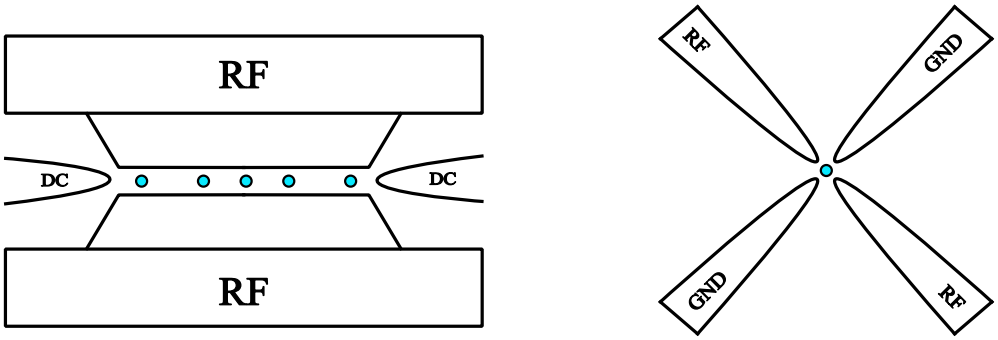

Figure 2.3: Schematic of the Linear Paul trap as seen from the radial and axial directions respectively

Observe that field is focusing along one axis, and defocusing along the other (ref eq. (2.8) and fig. 2.2b). This problem can be overcome by 'rotating' the field periodically, i.e., time modulating the applied voltages. This forces each axis to go into cycles of focusing/defocusing resulting in a net entrapment of the charged particle. This is formalised by writing the time-dependent RF potential as:

$$\Phi_{radial}(x,y,t) = \Phi(x,y)\cos(\Omega_{\mathrm{RF}}t) \tag{2.9}$$

where Ω_{RF} is the frequency of the applied RF voltage. The parameters for a dynamically stable trapping can be derived by solving the Mathieu equations (see eq. (2.14)).

2.2.2 Axial Harmonic Field

To achieve stable trapping of the ions in 3D, a static DC potential is applied for axial confinement. The endcap electrodes are used for this purpose where a DC voltage is applied.

$$\Phi_{axial}(z) = \frac{V_{\mathrm{DC}}}{L^2}z^2 \tag{2.10}$$

where V_{DC} is the applied DC voltage and L is the half-distance between the endcap electrodes. We can apply a paraxial approximation to this potential to get a approximated 3D harmonic potential. Consider the Taylor expansion of the potential around the trap axis (0,0,z):

$$\Phi_{axial}(\rho,z) \approx a_0(z) + a_1(z)\rho + a_2(z)\rho^2 + a_3(z)\rho^3 ... \tag{2.11}$$

where $\rho = \sqrt{x^2+y^2}$.

Since the potential is minimum at the axis, the linear term vanishes ($a_1(z) = 0$). Also due to the cylindrical symmetry of the trap, only even powered terms remain. We can further put this in the Laplace equation to get the values of the coefficients, where we get:

$$a_0(z) = \Phi_{axial}(z), \quad a_2(z) = -\frac{1}{4}\frac{d^2\Phi_{axial}}{dz^2}$$

Thus we get the paraxial approximation upto second order as:

$$\begin{aligned}\Phi_{axial}(\rho,z) &\approx \Phi_{axial}(z) - \frac{1}{4}\frac{d^2\Phi_{axial}}{dz^2}\rho^2 \\ &\approx \frac{\alpha V_{DC}}{L^2}\left[z^2 - \frac{1}{2}\left(x^2+y^2\right)\right]\end{aligned} \tag{2.12}$$

Here, $\alpha\,(<1)$ is the geometric factor specific to the trap configuration. Now we have sorted the axial confinement, but this also introduces a defocusing effect in the radial plane (see eq. (2.12)). Thus we need to form a combined potential that accounts for both the RF radial potential and DC axial potential.

2.2.3 Combined Mathieu Equations

With the axial and radial potentials defined in eq. (2.12) and eq. (2.9) respectively, we can write the total potential in the trap as:

$$\Phi(x,y,z,t) = \frac{\alpha V_{\mathrm{DC}}}{L^2}\left[z^2 - \frac{1}{2}\left(x^2+y^2\right)\right] + \frac{\Phi_0}{2r_0^2}(x^2-y^2)\cos(\Omega_{\mathrm{RF}}t) \tag{2.13}$$

Note that the potentials satisfy the Laplace equation $\Delta\Phi = 0$ independently. hence the sum follows too. From Newton's second law ($F = -e\boldsymbol{\nabla}\Phi$) it can be derived for a single ion of mass

m and charge e that:

$$\ddot{x} + \left[2\left(\frac{2e\Phi_0}{mr_0^2\Omega_{RF}^2}\right)\cos\Omega_{RF}t - \left(\frac{-4e\alpha V_{DC}}{mL^2\Omega_{RF}^2}\right)\right]\frac{\Omega_{RF}^2}{4}x = 0$$

$$\ddot{y} + \left[-2\left(\frac{-2e\Phi_0}{mr_0^2\Omega_{RF}^2}\right)\cos\Omega_{RF}t - \left(\frac{-4e\alpha V_{DC}}{mL^2\Omega_{RF}^2}\right)\right]\frac{\Omega_{RF}^2}{4}y = 0$$

$$\ddot{z} + \left[0 + 2\left(\frac{-4e\alpha V_{DC}}{mL^2\Omega_{RF}^2}\right)\right]\frac{\Omega_{RF}^2}{4}z = 0$$

Combining the constants, we can write these equations in the canonical form of Mathieu equations as:

$$\ddot{u}_i + [a_i + 2q_i\cos(\Omega_{RF}t)]\frac{\Omega_{RF}^2}{4}u_i = 0 \tag{2.14}$$

where u_i represents the position of the ions along the i^{th} axis ($i = x, y, z$) and the Mathieu parameters are defined as:

$$a_x = a_y = -\frac{1}{2}a_z = \frac{-4e\alpha V_{DC}}{mL^2\Omega_{RF}^2} \tag{2.15}$$

$$q_x = -q_y = q = \frac{2e\Phi_0}{mr_0^2\Omega_{RF}^2}, \quad q_z = 0 \tag{2.16}$$

We obtain stable trapping solutions [24] for the range $0 < q < 0.908$ and $|a| \ll 1$. In this regime, we can approximate the solutions of eq. (2.14) to be amplitude modulated harmonic oscillations given by:

$$u_i(t) \approx U_i\cos(\omega_i t)\left[1 + \frac{q_i}{2}\cos(\Omega_{RF}t)\right] \tag{2.17}$$

where U_i is the secular amplitude and ω_i is the *secular frequency*. From eq. (2.17), we can see that the ion's motion consists of a slow secular motion at frequency ω_i modulated by a fast *micromotion* at the RF frequency Ω_{RF}. The micromotion amplitude is proportional to the secular amplitude (displacement from the RF null) and is scaled by the stability parameter $q_i/2$.

The secular frequencies along the three axes are given by:

$$\omega_i = \frac{\Omega_{\mathrm{RF}}}{2}\sqrt{\frac{q_i^2}{2} + a_i}, \quad \text{where } i = x, y, z \tag{2.18}$$

Note, that since a_x and a_y are negative (in contrast to a_z, where it is positive and enables trapping), the axial trapping has a defocusing effect in the radial plane. The radial secular frequencies $\omega_r \equiv \omega_x = \omega_y$ is thus lower than what it would be without axial confinement. All operating parameters and the trap design used in this thesis will be discussed in chapter 3.

2.3 Laser Ion Interactions

Trapped ions are manipulated and interrogated using laser light. The interaction of laser light with the internal states of the ion allows for state preparation, manipulation, and measurement. In this section, we discuss the fundamental principles of laser-ion interactions, including the mechanisms of excitation, and coherent control.

2.3.1 Light-matter interaction

Consider a two-level atomic system (see fig. 2.5) with ground state $|g\rangle \equiv [1 \quad 0]^T$ and excited state $|e\rangle \equiv [0 \quad 1]^T$, separated by an energy difference $\hbar\omega_0$. The Hamiltonian for this system is given by:

$$H_0 = \frac{\hbar\omega_0}{2}\sigma_z \tag{2.19}$$

where σ_z is the Pauli-Z matrix.

When this two-level system interacts with a classical monochromatic electric field (laser light) of frequency ω_L, phase ϕ_L, and amplitude E_0, the interaction Hamiltonian in the dipole approximation[1] is given by:

$$\begin{aligned}
H_{int} &= -\vec{d}\cdot\vec{E}(t) \\
&= \begin{bmatrix} 0 & -\vec{d}_{ge}\cdot\vec{E}(t) \\ -\vec{d}_{eg}\cdot\vec{E}(t) & 0 \end{bmatrix} \\
&= \begin{bmatrix} 0 & \langle g|\boldsymbol{r}|e\rangle \\ \langle e|\boldsymbol{r}|g\rangle & 0 \end{bmatrix} e E_0 \cos(\omega_L t + \phi_L) \\
&= \hbar\Omega\cos(\omega_L t + \phi_L)\begin{bmatrix} 0 & 1 \\ 1 & 0 \end{bmatrix} \\
&= \hbar\Omega\cos(\omega_L t + \phi_L)\sigma_x
\end{aligned}$$

[1] also valid for our quadrupole qubit transition with a modified Ω (see eq. (2.32))

where $\vec{d} = e\vec{r}$ is the dipole moment operator, $\Omega = \frac{e\langle g|\boldsymbol{r}|e\rangle E_0}{\hbar}$ is the coupling strength of the levels, and $\vec{E}(t) = E_0\cos(\omega_L t + \phi_L)$ is the electric field of the laser. Thus, the total Hamiltonian of the system is:

$$H = H_0 + H_{int} = \frac{\hbar\omega_0}{2}\sigma_z + \hbar\Omega\cos(\omega_L t + \phi_L)\sigma_x \tag{2.20}$$

2.3.2 Rabi Oscillations and Single Qubit Gates

To simplify the analysis, we calculate the interaction Hamiltonian with H_0. The interaction picture Hamiltonian is:

$$H_I = e^{iH_0 t/\hbar} H_{int} e^{-iH_0 t/\hbar} \tag{2.21}$$

Calculating this, we find:

$$H_I = \hbar\Omega\cos(\omega_L t + \phi_L)\left(\sigma_+ e^{i\omega_0 t} + \sigma_- e^{-i\omega_0 t}\right) \tag{2.22}$$

where $\sigma_\pm = \sigma_x \pm i\sigma_y$ are the raising and lowering operators. Further simplifying by expanding the cos terms in the Euler form and using the rotating wave approximation (RWA), we neglect the rapidly oscillating terms [$(\omega_0 + \omega_L)$t] and obtain:

$$H_I \approx \frac{\hbar\Omega}{2}\left(\sigma_+ e^{-i(\Delta t - \phi_L)} + \sigma_- e^{i(\Delta t + \phi_L)}\right) \tag{2.23}$$

where $\Delta = \omega_L - \omega_0$ is the laser detuning from ω_0 (see fig. 2.5). This Hamiltonian can be intuitively understood as describing two possible processes: the absorption of a photon (σ_+) from the laser field, which excites the system from $|g\rangle$ to $|e\rangle$, OR the emission of a photon (σ_-), which de-excites the system from $|e\rangle$ to $|g\rangle$.

Now, for the case of resonant excitation ($\Delta = 0$) and $\phi_L = 0$, the time evolution operator in the interaction picture is given by:

$$U_I(t) = \exp\left(-\frac{i}{\hbar}H_I t\right) = \cos\left(\frac{\Omega t}{2}\right)I - i\sin\left(\frac{\Omega t}{2}\right)\sigma_x \tag{2.24}$$

Comparing with eq. (2.3), we see that this is equivalent to a rotation of the Bloch sphere vector about the x-axis by an angle $\theta = \Omega t$. The phase ϕ_L of the laser can be adjusted to achieve rotations about different axes in the xy-plane. Thus, by controlling the **duration**, **intensity**, and **phase** of the laser pulse, we can implement arbitrary single-qubit rotations.

For the case of near-resonant excitation ($\Delta \neq 0 \ll \Omega$), we apply eq. (2.22) to a general qubit state $|\psi(t)\rangle = c_1(t)|g\rangle + c_2(t)|e\rangle$ and solve the time-dependent Schrödinger equation to find

the time evolution of the state given by:

$$i\dot{c}_1 = c_2 e^{i\Delta t}\frac{\Omega}{2}$$
$$i\dot{c}_2 = c_1 e^{-i\Delta t}\frac{\Omega^*}{2} \tag{2.25}$$

Solving these coupled differential equations with initial condition that only $|g\rangle$ is populated ($c_1(0) = 1, c_2(0) = 0$), we find that the probability of measuring state of the system to be in $|e\rangle$ at time t is given by:

$$|c_2(t)|^2 = \frac{\Omega^2}{\Omega'^2}\sin^2\left(\frac{\Omega'}{2}t\right) \tag{2.26}$$

where $\Omega' = \sqrt{\Omega^2 + \Delta^2}$ is the generalized **Rabi frequency**. This shows that the population evolves periodically between both the states at a frequency determined by both the coupling strength and the detuning.

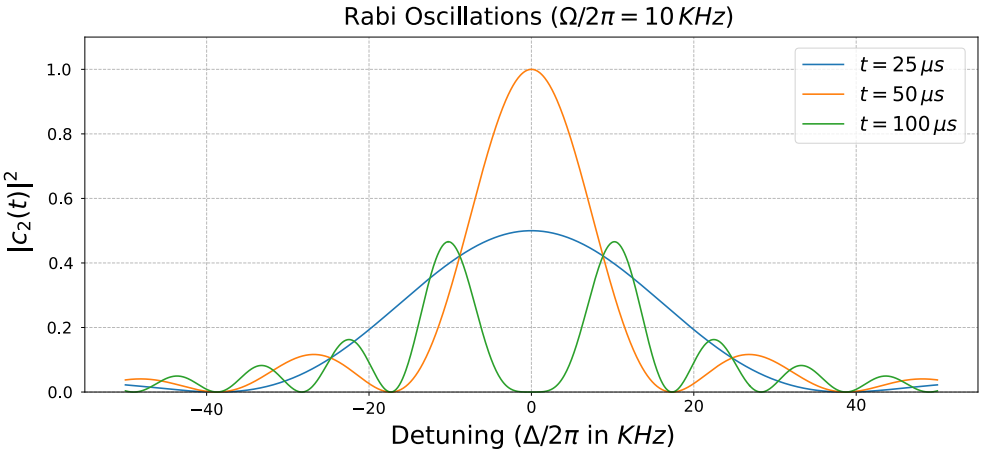

(a) Frequency domain plot as a function of detuning Δ for different probe times t

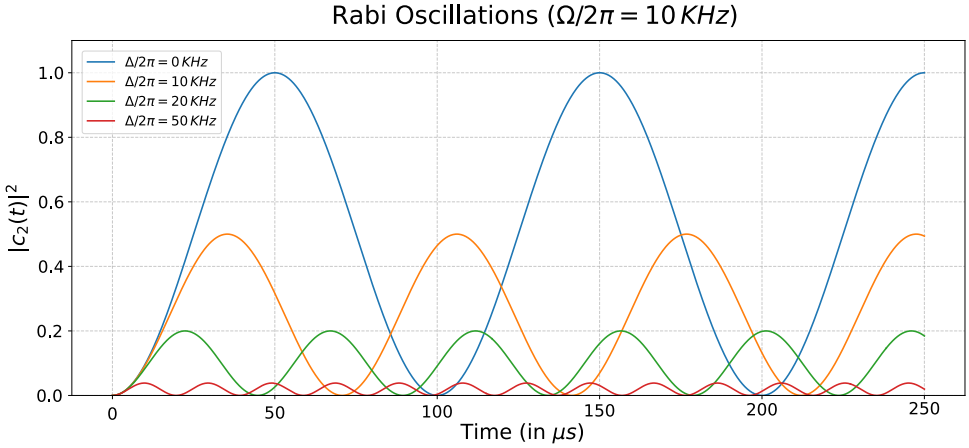

(b) Time domain plot as a function of probe time t for different detuning Δ

Figure 2.4: Population dynamics of the excited state $|e\rangle$ according to eq. (2.26)

From fig. 2.4b, we see that on resonance ($\Delta = 0$), there is maximum population transfer from the ground state to the excited state. The frequency of this population dynamics is the Rabi frequency Ω. As the detuning Δ increases, the oscillation frequency increases to the generalized Rabi frequency Ω', and the amplitude of the oscillations decreases by a factor of $\frac{\Omega}{\Omega'}$.

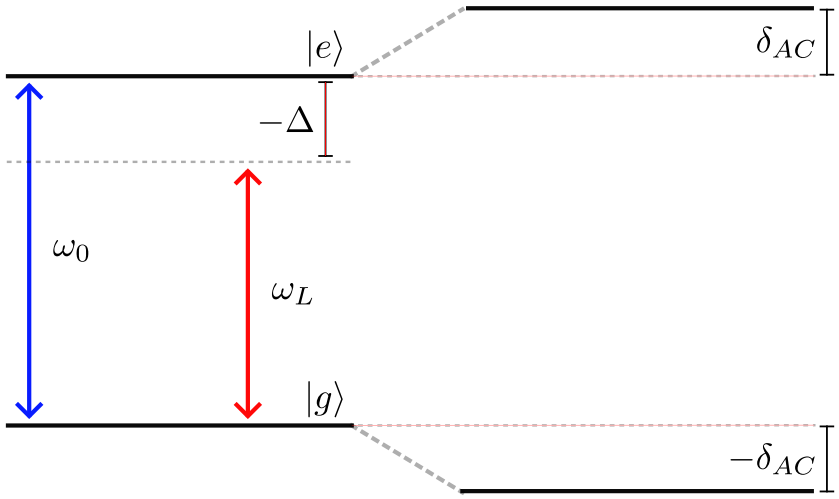

Figure 2.5: Light and a two level system interaction, showing the ground state $|g\rangle$, excited state $|e\rangle$, detuning Δ and AC Stark shift δ_{AC}.

For far-resonant excitation ($\Delta \gg \Omega$), the population transfer to the excited state is minimal, but it induces an energy shift in the levels known as the **AC Stark shift** or **light shift** because of the dynamic electric field of a laser. This shift can be derived using second-order perturbation theory and is given by:

$$\Delta E_g = \frac{\hbar\Omega^2}{4\Delta} = \delta_{AC}, \quad \Delta E_e = -\delta_{AC} \tag{2.27}$$

thus, the transition frequency is shifted by:

$$\Delta\omega_{AC} = -\frac{\Omega^2}{2\Delta} \tag{2.28}$$

This shift can be used as a phase gate [26] since it interacts with the σ_z operator scaled by the Light shift ($\frac{\hbar\Omega^2}{4\Delta}$). The time evolution operator for this interaction is given by:

$$\begin{aligned} U_{AC}(t) &= \exp\left(-\frac{i}{\hbar}H_{int}t\right) = \exp\left(-i\frac{\Delta\omega_{AC}}{2}\sigma_z t\right) \\ &= \cos\left(\frac{\Delta\omega_{AC}t}{2}\right) I - i\sin\left(\frac{\Delta\omega_{AC}t}{2}\right)\sigma_z \end{aligned} \tag{2.29}$$

Comparing eq. (2.29) with eq. (2.3) we see that is equivalent to a rotation of the Bloch sphere vector about the z-axis by an angle $\theta = \Delta\omega_{AC}t$. Thus, by controlling the **duration** and **intensity** of a far-detuned laser pulse, we can implement arbitrary phase gates.

2.4 Quantum Computation with Trapped Ions

In the previous sections, we discussed the fundamental principles of trapping ions and manipulating their internal states using lasers within a simple two-level interacting system framework. In real experimental setups, however, ions possess multiple motional modes due to the harmonic trapping potential, and the internal structure of ions often involves more than two energy levels. We first have a brief look at the level structure of the $^{40}Ca^{+}$ ion used in our experiments and how it is modified by external fields and trapping potentials. Then, we discuss how the motional modes of trapped ions can be used for quantum information processing (QIP).

2.4.1 Level Structure of $^{40}Ca^{+}$

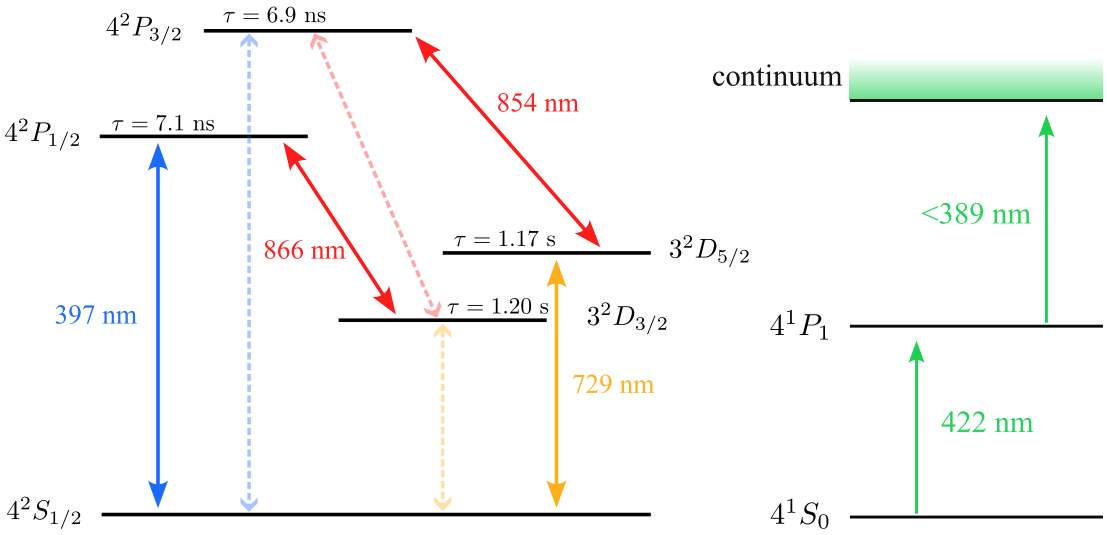

(a) $^{40}Ca^{+}$ ion relevant energy levels (b) Ca atom relevant energy levels

Figure 2.6: Dashed blue, red and yellow transitions are 393 nm, 850 nm and 732 nm respectively, which are not laser driven in our experiments. Solid lines indicate transitions which are driven using lasers. Transitions wavelengths and lifetimes are taken from [27, 28].

The $^{40}Ca^{+}$ ion has a Hydrogen-like internal level structure, with a single valence electron. The most relevant levels for QIP are the ground state $^2S_{1/2}$, the metastable state $^2D_{5/2}$, and the excited state $^2P_{1/2}$. The $^2P_{1/2}$ state has a branching ratio of approximately 94 % to the ground state and 6 % to the $^2D_{3/2}$ state, thus the $^2D_{3/2}$ state also becomes practically relevant. The

qubit is encoded in the long-lived ($\tau \sim 1.17$ s [29]), ultra-narrow ($\Delta\nu \sim 0.14$ Hz) $^2S_{1/2} \leftrightarrow ^2D_{5/2}$ transition.

External magnetic fields are applied to lift the degeneracy of the Zeeman sublevels, allowing for precise control over the qubit states. A magnetic field is crucial for breaking the degeneracy of the Zeeman sublevels. If not broken, the ion would be in a superposition of the sublevels called CPT dark states, which results in the ions not interacting with the detection beam, or having different coupling strengths to the 729 nm beam, which leads to reduced state detection fidelity and rabi frequencies. A qubit transition with degenerate sublevels can lead to increased decoherence. It also has to be noted that too much Zeeman splitting can lead to reduced doppler cooling efficiency due to the broadening of cooling transition. The energy splitting for the relevant levels under an external magnetic field B is given by the Zeeman effect:

$$\Delta E = g_J m_J \mu_B B, \tag{2.30}$$

The Landé g-factor is given by the formula:

$$g_J = 1 + \frac{J(J+1) + S(S+1) - L(L+1)}{2J(J+1)}, \tag{2.31}$$

using which, we obtain the g-factors for the relevant levels as $g_{^2S_{1/2}} = 2$ and $g_{^2D_{5/2}} = 6/5$.

To find the relative transition strengths between the Zeeman sublevels of the $^2S_{1/2} \leftrightarrow ^2D_{5/2}$ transition, we calculate the squared Clebsch-Gordan coefficients for the allowed transitions. In our case, the involved transitions are quadrupole transitions with selection rules $\Delta m_J = 0, \pm 1, \pm 2$. The associated Rabi frequencies for each transition are proportional to the Clebsch-Gordan coefficients, which determine the relative line strengths. The rabi frequencies are given by [30]

$$\Omega_{m_J, m_{J'}} = \Omega_0 \kappa(J, m_J; J', m_{J'}) c_{ij}^{(\Delta m)} \varepsilon_i \boldsymbol{n}_j \tag{2.32}$$

where

$$\Omega_0 = \frac{ekE}{2\hbar\sqrt{2J'+1}} \langle nJ || r^2 C^{(2)} || n'J' \rangle, \tag{2.33}$$

with E being the electric field amplitude of the addressing laser, and $\langle nJ || r^2 C^{(2)} || n'J' \rangle$ being the reduced matrix element for the quadrupole operator between the initial and final states. The term $\kappa(J, m_J; J', m_{J'})$ is the Clebsch-Gordan coefficient for the transition from state (J, m_J) to $(J', m_{J'})$ given by:

$$\kappa(J, m_J; J', m_{J'}) = \sqrt{2J'+1} \begin{pmatrix} J & 2 & J' \\ -m_J & \Delta m & m_{J'} \end{pmatrix} \tag{2.34}$$

The coefficients $c_{ij}^{(\Delta m)}$ represent rank-2 quadrupole tensor for Δm. The vector $\boldsymbol{n}$ denotes unit vector along the wavevector k and ε_i is the polarization vector. The orientation of the laser

beam relative to the magnetic field determines the polarization components ε_i and the direction $\boldsymbol{n}_j$.

Plots below (fig. 2.7) illustrate the geometric strength factors for different laser beam orientations and polarizations with respect to magnetic field.

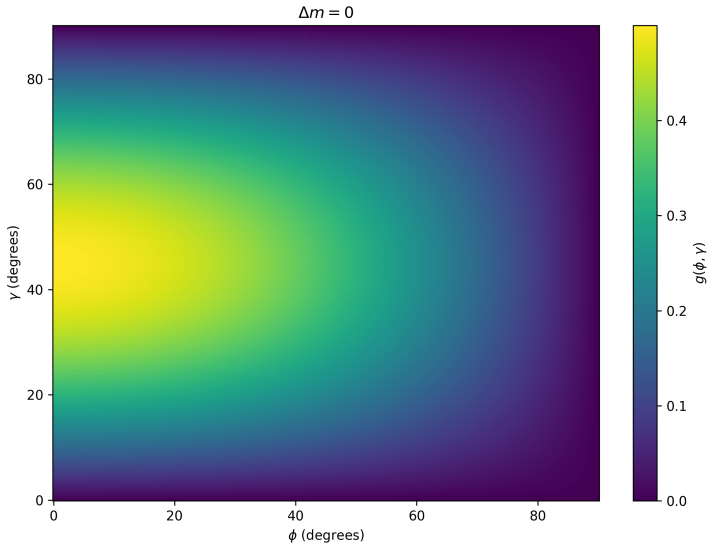

(a) $\Delta m = 0$ transitions

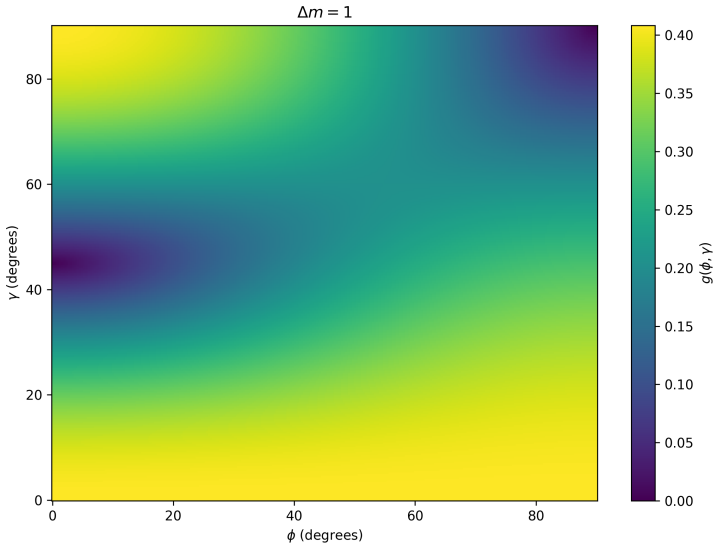

(b) $\Delta m = 1$ transitions

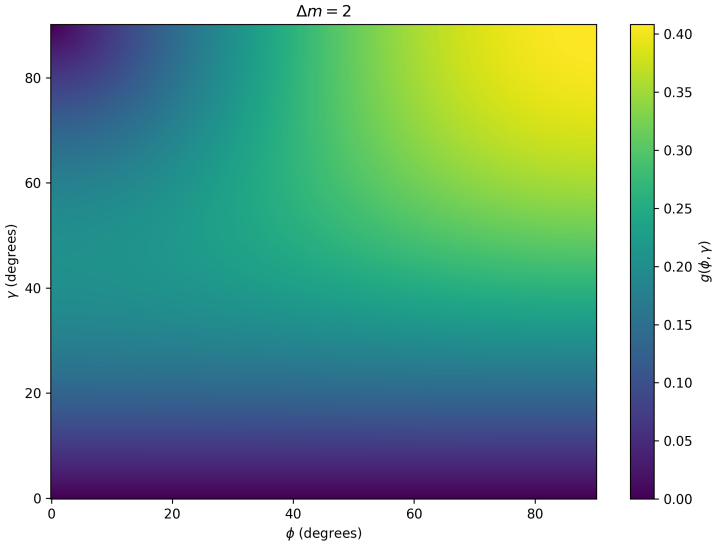

(c) $\Delta m = 2$ transitions

Figure 2.7: Geometric coupling strengths for quadrupole transitions in $^{40}Ca^{+}$ ion as a function of laser beam orientation ϕ and polarization angle γ. Expression for $g(\phi, \gamma)$ are given in [31]

Using eq. (2.30) to calculate the energy shifts (fig. 2.8a) for the $^2S_{1/2}$, $^2D_{5/2}$ states and subsequently the transition lines, we plot a carrier transition spectrum as in fig. 2.8b.

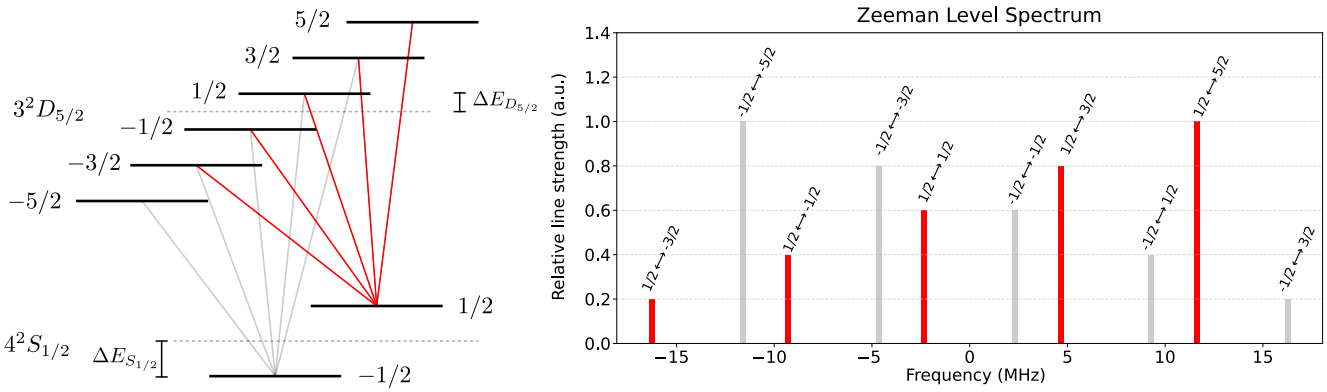

(a) Zeeman splitting of relevant levels

(b) Transition line spectrum for all allowed lines

Figure 2.8: Red denotes the $m_j = 1/2$ transitions which are used in our experiments. Zero point refers to the non-splitted line (dotted levels). The splitting is calculated for a magnetic field of $B = 4.1$ G. Line strengths are given by squared Clebsch-Gordan coefficients from eq. (2.34).

2.4.2 Effect of Harmonic trapping potential

As we saw in section 2.2.3, the primary motion of ions is characterized by confinement in a pseudo-harmonic potential with frequencies along the axes given by eq. (2.18). This harmonic confinement leads to quantized motional states for the ions, which can be described using quantum harmonic oscillator formalism. The motional states are represented by Fock states $|n\rangle$, where n is the motional quantum number. The energy levels of the motional states are given by:

$$E_n = \hbar\omega_r \left(n + \frac{1}{2}\right), \tag{2.35}$$

corresponding to the trap Hamiltonian,

$$H_{trap} = \hbar\omega_r \left(a^\dagger a + \frac{1}{2}\right), \tag{2.36}$$

where ω_r is the secular frequency of the trap along a given axis. Thus, eq. (2.19) is now:

$$H_0 = \frac{\hbar\omega_0}{2}\sigma_z + H_{trap} \tag{2.37}$$

The interaction Hamiltonian corresponding to laser-ion interaction as defined in eq. (2.22) is modified in the presence of motional states as:

$$H_{int} = \hbar\frac{\Omega}{2}\sigma_x \left(e^{i\left(\vec{k}\cdot\vec{r} - \omega_L t + \phi_L\right)} + h.c.\right), \tag{2.38}$$

where ω_L is the frequency of the laser. The term $\vec{k}\cdot\vec{r}$ represents the coupling between the internal states and the motional states, where $\vec{k}$ is the beam wavevector and $\vec{r}$ is the ion's position operator. The position operator can be written in the ladder operator formalism of the harmonic oscillator as $\vec{r} = \sqrt{\frac{\hbar}{2m\omega_r}}(a + a^\dagger)$, where ion mass is given by m. Here we define,

$$\eta = k\cos\phi\sqrt{\frac{\hbar}{2m\omega_r}} \tag{2.39}$$

as the Lamb-Dicke parameter, quantifying the coupling strength between the electronic bare states and the oscillator states. Writing this in the interaction picture with respect to H_0 as in eq. (2.38) and using the rotating wave approximation, we have:

$$H_I = \hbar\frac{\Omega}{2}\left(e^{-i(\Delta t-\phi_L)}\sigma_+ e^{i\eta(ae^{-i\omega_r t}+a^\dagger e^{i\omega_r t})} + h.c.\right) \tag{2.40}$$

Similar to how a two-level system's interaction with the quantized EM field [32] leads to various light-dressed states depending on the photon number states, the interaction of the electronic bare states with its vibrational states leads to a set of combined states $|g,n\rangle$ and $|e,n\rangle$, where n is the motional quanta of the ion in the trap potential. Due to the different vibrational degrees of freedom, it can not only absorb an incoming photon of frequency ω_0 but also $\omega_0 \pm n\omega_r$. Transitions between these combined states can be driven using lasers, leading to mainly three types of transitions:

- Carrier transition: $|g,n\rangle \leftrightarrow |e,n\rangle$, where the motional state remains unchanged. This corresponds to the case where the laser is resonant with the internal transition frequency ($\Delta = 0$).
- Red sideband transition: $|g,n\rangle \leftrightarrow |e,n-1\rangle$, where the ion absorbs a photon and loses one motional quantum (from $|g,n\rangle$). This occurs when the laser is detuned by $-\omega_r$ from the internal transition frequency ($\Delta = -\omega_r$).
- Blue sideband transition: $|g,n\rangle \leftrightarrow |e,n+1\rangle$, where the ion absorbs a photon and gains one motional quantum (from $|g,n\rangle$). This occurs when the laser is detuned by $+\omega_r$ from the internal transition frequency ($\Delta = +\omega_r$).

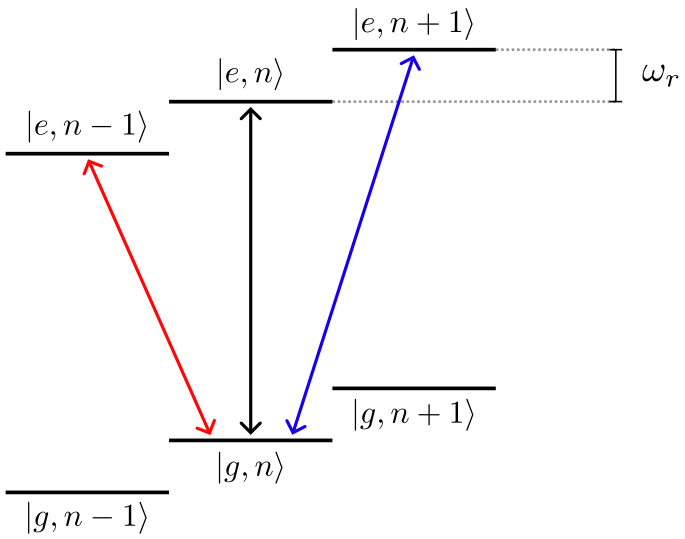

We define the Lamb-Dicke regime as the regime where $\eta^2(2n+1) \ll 1$, which corresponds to the case where the ion position's gaussian wave-packet is restricted to a region much smaller than the wavelength of the laser. It can also thought of as a condition which imposes that the recoil energy is much smaller than the trap frequency. In this regime, we can expand the exponential term in the interaction Hamiltonian as:

$$e^{i\eta(ae^{-i\omega_r t}+a^\dagger e^{i\omega_r t})} \approx 1 + i\eta(ae^{-i\omega_r t} + a^\dagger e^{i\omega_r t}) \tag{2.41}$$

This approximation allows us to separate the interaction Hamiltonian into three distinct parts corresponding to the carrier, red sideband, and blue sideband transitions:

$$\begin{aligned} H_I^{carrier} &= \hbar\frac{\Omega_{n,n}}{2}\left(e^{-i(\Delta t-\phi_L)}\sigma_+ + h.c.\right) \\ H_I^{red} &= i\hbar\eta\frac{\Omega_{n,n-1}}{2}\left(e^{-i((\Delta+\omega_r)t-\phi_L)}a\sigma_+ + h.c.\right) \\ H_I^{blue} &= i\hbar\eta\frac{\Omega_{n,n+1}}{2}\left(e^{-i((\Delta-\omega_r)t-\phi_L)}a^\dagger\sigma_+ + h.c.\right) \end{aligned} \tag{2.42}$$

Rabi frequencies for the carrier and sideband transitions are given by:

$$\begin{aligned} \Omega_{n,n} &= \Omega(1-\eta^2 n) \\ \Omega_{n,n-1} &= \eta\Omega\sqrt{n} \\ \Omega_{n,n+1} &= \eta\Omega\sqrt{n+1} \end{aligned} \tag{2.43}$$

Chapter 3

Experimental setup and methods

This chapter extensively describes the experimental setup and methods used in this thesis. We start with a detailed description of the linear Paul trap, its design and construction, followed by a discussion on the experimental setup, including the vacuum layout, optical layout, and control electronics. We also discuss the methods used for ion loading, cooling, and state manipulation, as well as the techniques used for state detection and measurement.

3.1 Trap Design, Electronics and Control

The trap is designed to have an ion-electrode distance of 0.8 mm, and an axial length of 5.6 mm. The endcaps are separated by 5.86 mm (as in fig. 3.1a), and the RF blades are separated by 1.6 mm (as in fig. 2.3). The radius of curvature of the blade edges is 0.1 mm. The RF Blades are made of titanium, while the endcaps are made of stainless steel. The RF blades are sputter coated with gold and endcaps are gold-coated by thermal vapour deposition. This minimizes patch potentials on the blade surfaces due to the chemically inert nature of gold.

The blades are assembled on a custom-designed Macor® holder, which is attached to the bottom of the vacuum chamber via a baseplate mounted on four rods. The chamber itself is a stainless steel octagon with 9 CF35 ports (including one on the recessed CF160 front flange) for optical access and feedthroughs. Using a reducer flange, this is attached to a three-way cross CF100 stainless steel body with ports for the ion pump, titanium sublimation pump and the angle valve for connecting Turbomolecular pump. The trap is mounted in the center of the octagon, with the RF and DC connections fed through the feedthroughs on the trap axis. Lasers are sent through the viewports for optical access. Imaging is done as well with this access.

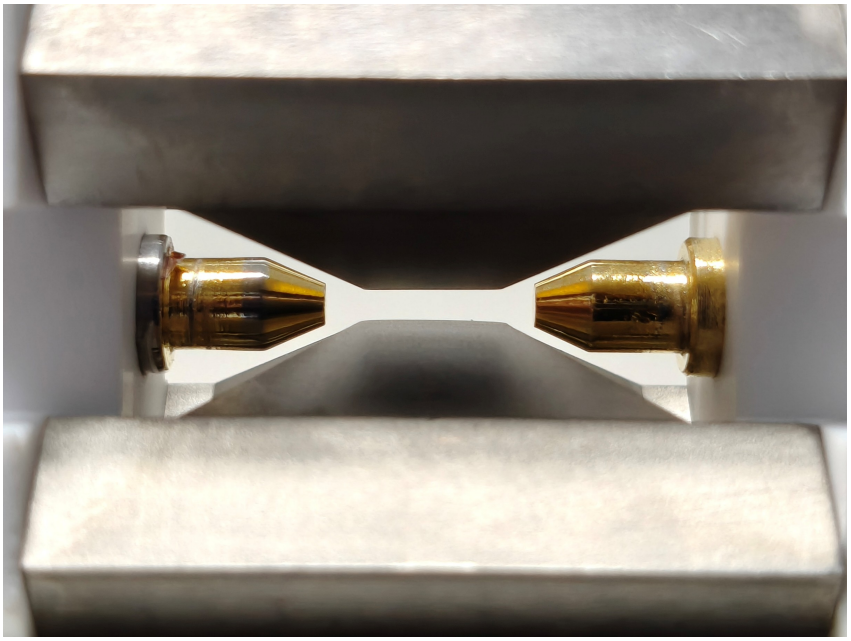

(a) Trap front view

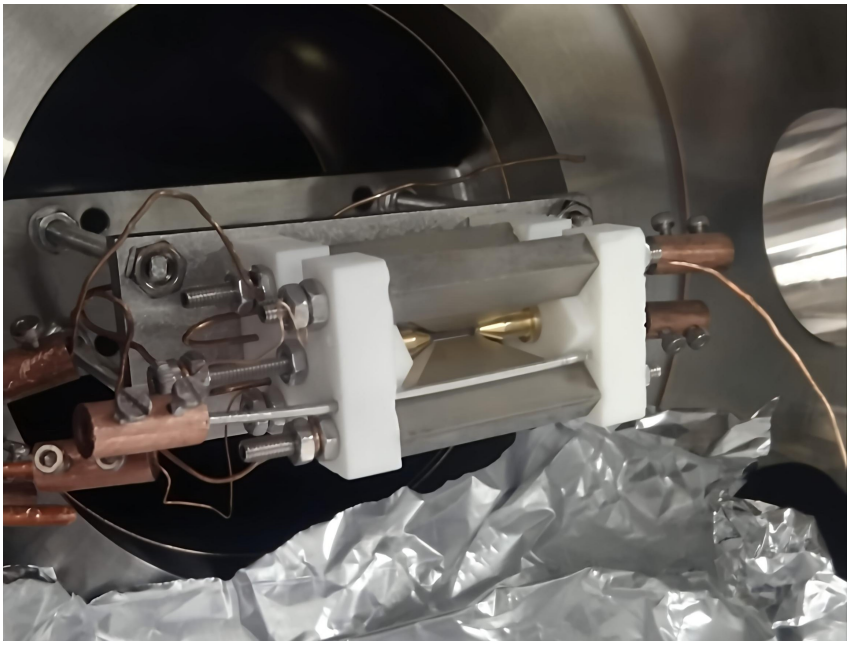

(b) Trap installed in the vacuum chamber

Figure 3.1: Actual images based on which schematics in fig. 2.3 are made (a) Chamber face view of the trap, with two of the blade electrodes and the endcaps visible. (b) The trap installed in the vacuum chamber with all the necessary connections to feedthroughs.

3.1.1 RF Drive and Resonator

The RF drive is generated by a VCO-based, HP 8656B Signal Generator and amplified by a MiniCircuits high power RF amplifier. We need voltages near $\sim$ 500 V at $\sim$ 20 MHz to create the desired radial trapping potential. To achieve this, we use a helical resonator which serves mainly three purposes:

- Impedance matching between the RF source and the trap for efficient power transfer and to prevent reflections that can damage the amplifier.
- Stepping up the voltage to the required levels, as the RF drive from the amplifier is typically in the range of a few volts, while the trap requires hundreds of volts for effective ion confinement.
- Acting as a bandpass RLC filter to suppress unwanted frequencies and noise from the RF drive, ensuring a clean signal for stable ion trapping.

Output of the amplifier is fed into the resonator via a bidirectional coupler, which allows us to monitor the reflected power from the trap to ensure proper impedence matching. The Signal Generator leads to the amplifier via a control box which has a voltage variable attenuator (taking inputs from ARTIQ DACs) and a TTL switch (taking inputs from ARTIQ DIOs) for switching and amplitude control of the RF drive. The amplified input to the resonator is $\sim$ 44 dbm, and we get an output in the range of 500-800 V in the trap[1]. In this thesis, we are working at a drive frequency of $\sim$ 19.77 MHz.

3.1.2 DC Voltage Control for Axial Confinement

The DC voltages for axial confinement are generated by iSEG SHR high voltage power supply. We have observed stable trapping from 150V to 900 V on the endcaps, which is more than sufficient for our experiments. We are limited by the voltage rating of the feedthrough, which is 1 kV. A low pass RC filter is used to filter out any possible high frequency RF pickup from the DC voltages before they are connected to the vacuum feedthroughs. The RC filter is made of a 220 kΩ resistor and a 0.1 μF capacitor, giving us a cutoff frequency of $\sim$ 7 Hz, which is sufficient to filter out any RF pickup at $\sim$ 20 MHz. The power supply is connected via ethernet to the control PC and controlled by the iCS control software.

[1]This is back calculated from the measured radial secular frequencies, refer chapter 4. This range is verified by measuring with a capacitive voltage divider.

3.1.3 Imaging System: High NA Objective and EMCCD

Efficient collection of fluorescence photons from the ion is crucial for high-fidelity state detection. Ions are imaged using *Sill Optics* S6ASS2258-006, a high NA (~ 0.4) objective lens with a working distance of ~ 60.5 mm and an image distance of ~ 422.5 mm, which is mounted right outside the recessed CF35 viewport on an XYZ stage for optimum alignment. The collected fluorescence is then focused onto an *Andor iXon Ultra* 897 EMCCD camera mounted on an XY stage.

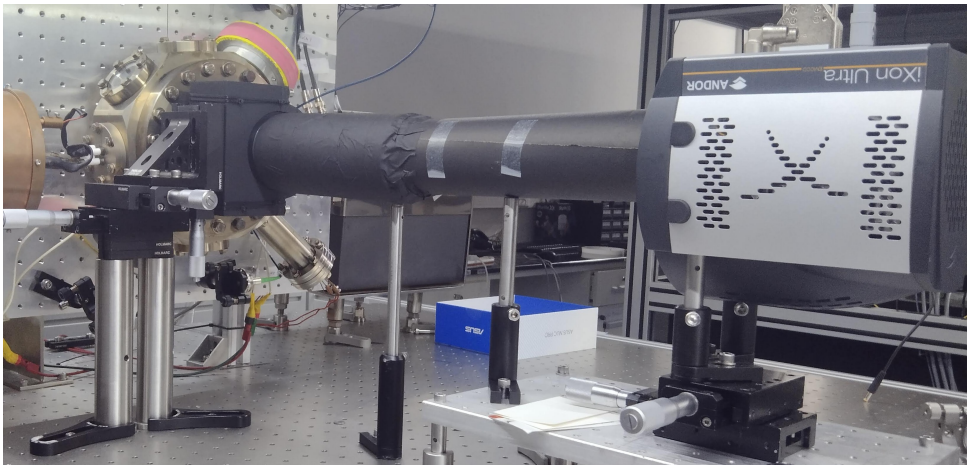

Figure 3.2: Imaging system setup showing the high NA objective and the EMCCD camera.

The tested magnification of the imaging lens is ~ 11 at the EMCCD plane, which gives us a field of view of ~ 0.55 mm^2 (considering its active pixel area of 512×512 and pixel size of 16 μm), more than sufficient for imaging linear ion chains. The camera is connected to the control PC via USB and controlled by the Andor Solis software for image acquisition and analysis. The region between the objective and the camera is covered (as shown in fig. 3.2) to block any stray light from reaching the camera. Typically, we work at an EM Gain of 300 and exposure times in the range of 10-50 ms for the initial image alignment and experiments as well.

3.1.4 Quantization Field Coils

A quantization magnetic field of ~ 4.16 G is applied[2] at the trap center using a pair of 70 mm diameter coils in a near-Helmholtz configuration at 1.46 A. The coils are made of copper wire of 1 mm diameter with 320 turns each and are driven by Delta Electronika power supply in constant current mode. The coils are designed to provide a uniform magnetic field (relative to extent of ion motion) at the trap center.

[2]not measured, but the calculated field. Further details in chapter 4

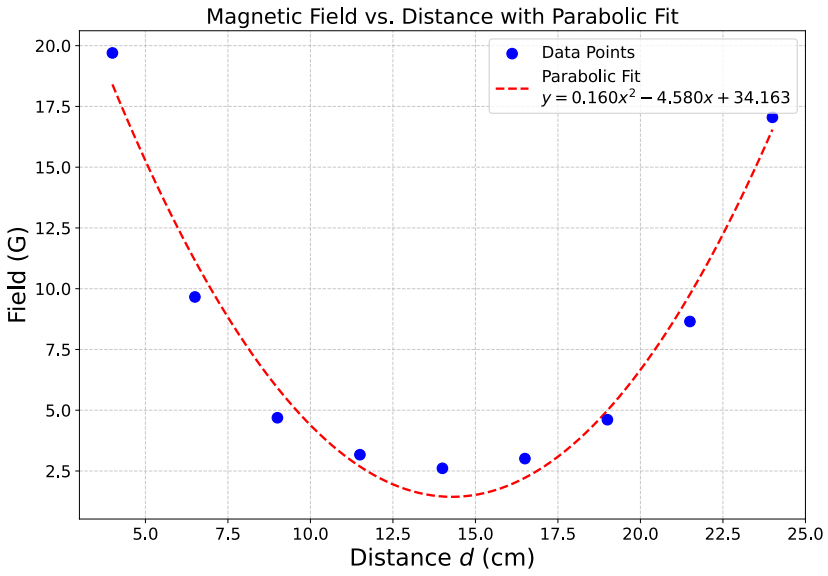

Figure 3.3: Magnetic field measurements for quantization coils at 1A current at inter-coil separation of 28 cm.

The field is measured using a gaussmeter before mounting, and the measurements are presented in fig. 3.3. The coils are mounted around diagonally opposite viewports, 45° to the trap axis. This is kept as such because, in this configuration, the field is at 45° to the 729 nm beam $\vec{k}$ vector, which ensures maximal coupling (refer fig. 2.7) to the $S_{1/2}(m_J = 1/2) \leftrightarrow D_{5/2}(m_J = 1/2)$ transition. This transition is used as the main qubit transition in this thesis since it's the least sensitive to $\vec{B}$ field noise among the various Zeeman transitions and thus is least prone to decoherence in this aspect.

3.1.5 Control System: ARTIQ

The entire experiment, barring a few devices (like the iSEG power supply and the Delta Elektronika power supplies for the calcium oven and the quantization field coils) is controlled by the *ARTIQ* control system. *ARTIQ* is an open-source software platform for controlling quantum information experiments with precise timing and synchronization. It is a python-based scripting environment, which is used to schedule precisely timed events from our host system, executed using *Sinara* hardware.

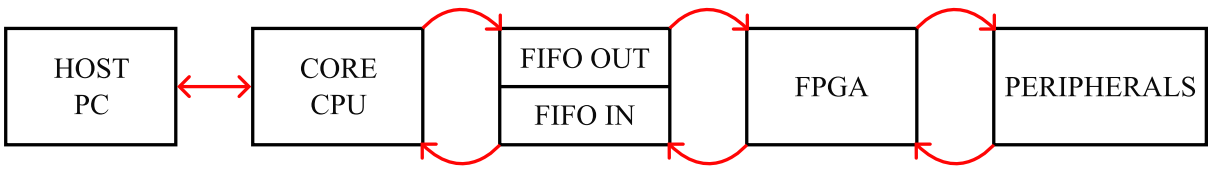

Figure 3.4: ARTIQ control system showing the Host PC, the FPGA core and the various peripherals attached to it.

Direct communication between CPU and the FPGA leads to unwanted latency errors. To counter this, the core CPU pushes timestamped instructions into a FIFO buffer, which serves as the interface between the Host PC and the FPGA core. Hardware events are decoupled from code execution by scheduling events in the future. These are later executed by the FPGA core when the system clock reaches the specified timestamp attached to an event, via various peripherals attached to the *Sinara* rack.

Main carrier card used in our *Sinara* rack is the 1125 *Kasli-SoC* which includes an FPGA and a CPU. The peripherals attached include the 4412 DDS *Urukul* for driving the AOMs, 2238 MCX-TTL card for digital input/outputs and 5528 SMA-IDC card for DAC outputs.

3.2 Laser Systems and Optical Layout

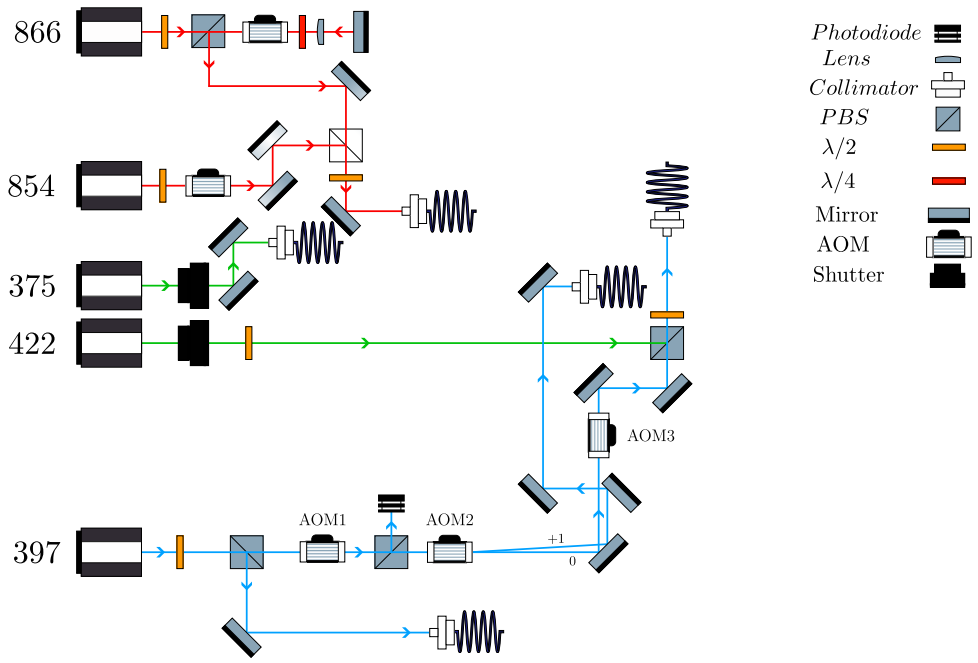

Figure 3.5: Laser systems and optical layout

3.2.1 Cooling and Photoionization Lasers

The red lasers denote the repumpers, green the photoionization and blue the doppler cooling. Acousto optic modulators (AOMs) are used for fast switching and frequency control of the beams. Except for the 866 nm path, all other lasers shown in the image are in single pass AOM configuration. The photoionization lasers do not require fast switching and are therefore not

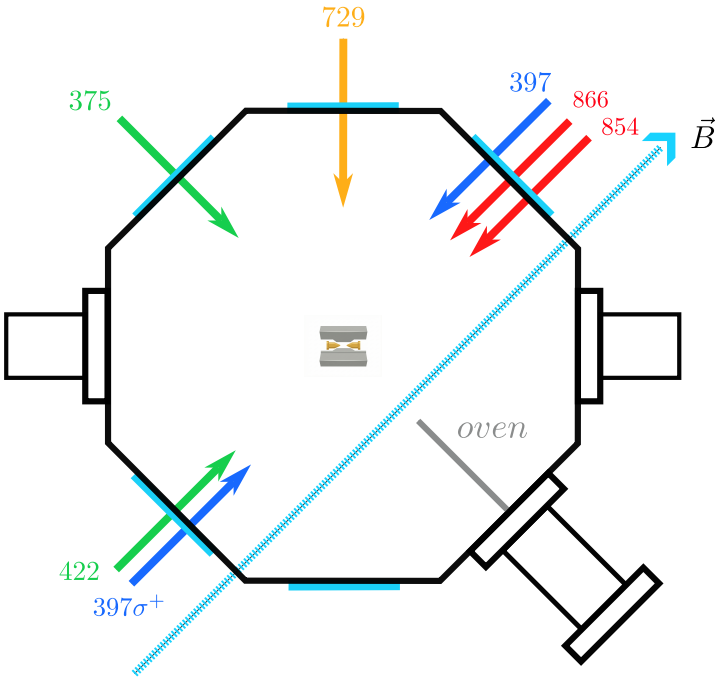

Figure 3.6: Vacuum chamber and beam geometry

passed through AOMs, rather mechanical shutters are used. Two shutters, each in front of the 375 nm and 422 nm laserheads, are controlled by the same DIO TTL.

The 397 nm laser is diverted into different paths. The reflected PBS path is used for a PID-based frequency lock using *HighFinesse* wavemeter. AOM1 in the transmitted path is used for intensity stabilization with a photodiode feedback. This path leads into AOM2, whose first order is sent for doppler cooling and detection, while the zero order is sent to AOM3, to be used for optical pumping. This configuration works well without power sacrifices since the optical pumping beam is never used simultaneously with the cooling/detection beam.

The optical pumping beam is mixed with the 422 nm photoionization beam using a PBS, and is coupled to a single fiber directly into the trap. The 375 nm beam is sent directly out of a separate fiber in a different path. Although the Doppler (397 nm) and repumper (854 nm, 866 nm) beams are coupled to different fibers, they are combined using a dichroic before being sent to the trap. This was done to avoid the polarization fluctuations that arise in 866 nm through the fiber.

3.2.2 Narrow linewidth laser for Quadrupole qubit transition (729 nm)

The 729 nm laser is used for qubit manipulation and is PDH-locked to a high finesse cavity for frequency stabilization. Additionally, we also have a fiber noise cancellation system in place to nullify frequency noise in the kHz range arising from the optical fibers. We get $\sim$ 120 mW of power out of the fiber dock to the experiment. This alone isn't sufficient for both single ion addressing and global addressing. So we split this into two paths as shown in fig. 3.7, one goes through a double pass AOM setup for global ion addressing, while the other goes

Figure 3.7: Global and single ion addressing optics for the 729 nm laser.

through TOPTICA's TA pro tapered amplifier system, out of which $\sim$ 500 mW is available (without accounting for AOM efficiency and fiber coupling loss) for single ion addressing. The amplified beam is then sent through a double pass AOM setup for frequency control before being focused onto the ion. Using a double pass AOM setup is critical for the 729 nm laser since we require a large frequency tuning range (in the order of 10 MHz) without sacrifices in laser power for doing spectroscopy on the qubit transition. We get a maximum of $\sim$ 85 mW out of the fiber for addressing, focused to a spot size of $\sim$ 300 μm at the ion. The absolute frequency of the laser post-double pass AOM at 300 MHz is 411.042129 THz. This is our zero field center frequency of the transition.

3.3 Loading and Trapping $^{40}Ca^{+}$ Ions

This section describes the methods used for loading and trapping $^{40}Ca^{+}$ ions in our linear Paul trap. We discuss the process of setting up UHV conditions, atomic oven, neutral atom fluorescence, initial imaging of the ion cloud, and more.

3.3.1 Vacuum system

Ultra-high vacuum (UHV) conditions are essential for ion trapping experiments to minimize collisions with background gas molecules, which can lead to ion loss and decoherence. All the components to be used inside the vacuum chamber are first cleaned using ultrasonic baths with soap solution, followed by acetone to remove any contaminants. Proper vacuum-safe protocols are followed while handling the components to avoid recontamination. The trap is then assembled outside and installed in the octagon, following which all the necessary electrical connections are made.

The entire vacuum system is covered with aluminum foil, wrapped with a glass-wool heating tape for bakeout. Typically, we bake the system at temperatures around 150 – 200 °C for a week to achieve the desired UHV conditions. The chamber is pumped down using a Turbomolecular pump backed by a dry scroll pump. Once we ramp down the temperature slowly and the pressure reaches $\sim 10^{-9}$ Torr, we start the ion pump and titanium sublimation pump to reach UHV conditions at $\sim 10^{-11}$ Torr. The turbo and Ti-sublimation pumps are disconnected before starting the experiment whereas the ion pump stays on always. The pressure is monitored using an ion gauge and a residual gas analyzer. A detailed description of the vacuum chamber system used in this thesis can be found in section 3.1.

3.3.2 Imaging system

The imaging system is described in detail in section 3.1.3. The system uses a high NA objective lens and an EMCCD camera to image the trapped ions. The trap is imaged coarsely on a white paper by shining a bright light on the trap through one of the viewports and adjusting the position of the objective to get an image of the trap center at the specified image distance for the recommended minimum working distance. The focus can be adjusted by crashing one of the beams on the trap and adjusting the objective position to get a sharp image of the beam spot on the trap. The EMCCD camera is then positioned here to get a focused image of the trap center, which is where we expect the ions to be trapped.

3.3.3 Neutral atom fluorescence

To load ions into the trap, we first need to create a beam of neutral calcium atoms. This is achieved using an atomic oven, which consists of a small reservoir filled with calcium metal. The oven is heated resistively to produce a vapor of neutral calcium atoms that can be directed towards the trap center. The oven filament is pointed towards the trap centre and its flux is

controlled by adjusting the current (via a Delta Elektronika power supply) through the filament. Typically, around ~ 6 A of current is passed for detecting fluorescence. Following this, we try to observe the 422 nm fluorescence which is useful for:

- Aligning the atomic beam, and the 422 nm beam with the trap center.
- Estimating the oven flux and optimizing it for efficient ion loading.
- Finding the resonance frequency of the 422 nm transition for efficient photoionization.

The $S_0 \leftrightarrow P_1$ transition of ^{40}Ca (see fig. 2.6b) is driven by the 422 nm laser. The laser's frequency is scanned around the approximate resonant frequency and the image on a CCD camera was observed with a standard Nikon camera lens (since it's easier to work with lower magnification), to find the resonance frequency of the transition. If the oven flux is sufficient and the 422 nm beam is well aligned, we can see a bright line of fluorescence on the CCD image as in fig. 3.8.

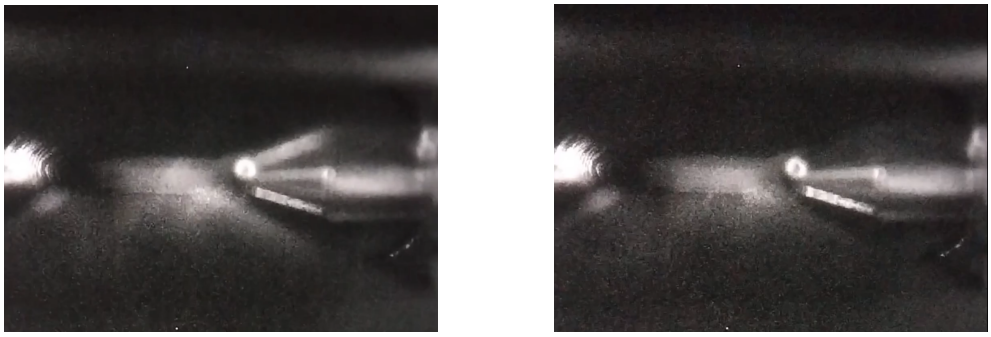

(a) CCD image with fluorescence (b) CCD image without fluorescence

Figure 3.8: Fluorescence from neutral calcium atoms seen on one of the endcaps when 422 nm is on and off resonance. The bright line in (a) is the fluorescence from the neutral calcium atoms, which disappears in (b) when the laser is off resonance.

Shifts in the order of a few hundred MHz can be expected with different orientations of the oven and the 422 nm beam, which can be attributed to the Doppler shift arising from the velocity distribution of the atomic beam. For instance, a resonance frequency of ≈ 709.0783 THz was observed when the oven is pointed at 45° to the 422 nm beam compared to ≈ 709.0787 THz when the oven is pointed at 90° (configuration used in this thesis as in fig. 3.6) to the 422 nm beam.

3.3.4 Photoionization

After observing the neutral atom fluorescence, we photoionize the neutral calcium atoms to load ions into the trap. Before that, we place an optical bandpass filter in front of the EMCCD camera to only let through the 397 nm fluorescence from the ions, which reduces background noise and improves detection fidelity. Here, photoionization is a two-step process, where the 422 nm beam drives the $S_0 \rightarrow P_1$ transition, and the 375 nm beam excites it to the continuum (see fig. 2.6b). The operating frequency and alignment of the 375 nm beam is not as crucial as the 422 nm, thus it's a free running laser. A few hundred μW of power in the 422 nm beam and a few mW of power in the 375 nm beam is found to be sufficient for efficient photoionization.

3.3.5 Doppler cooling and detection

The 397 nm laser drives the $S_{1/2} \leftrightarrow P_{1/2}$ transition of $^{40}Ca^{+}$ which is used for both cooling and detection. This transition has a linewidth of ≈ 20 MHz, which allows for efficient cooling of the ions to near the Doppler limit. Additionally, the fluorescence from this transition can be collected and imaged onto the EMCCD camera for imaging of ions. Since the $P_{1/2}$ state has a small branching ratio (refer section 2.4.1) with which it can decay to the metastable $D_{3/2}$ state (which is not addressed by the 397 nm laser), we use an 866 nm repumper laser to drive the $D_{3/2} \leftrightarrow P_{1/2}$ transition to prevent population from getting trapped in the $D_{3/2}$ state over multiple cooling cycles, enabling continuous cooling and fluorescence detection.

Doppler cooling is most effective when the the $\vec{k}$ of 397 nm has a non-zero projection onto all the ion's motional axes. In our setup as shown in fig. 3.6, the 397 nm beam is at 45^0 to the trap axis, which ensures that it has components along both the axial and radial directions, allowing for efficient cooling in all directions. Further, the cooling rate is maximum when the laser is detuned to the red side by half a linewidth, which is ≈ 10 MHz for the cooling transition in $^{40}Ca^{+}$. We typically operate the 397 nm beam with ~ 250 μW of power at a frequency of $\approx$ 755.22265 THz with a detuning of around 10 – 15 MHz. The 866 nm frequency is $\approx$ 346.0001 THz at a power of ~ 1 mW.

3.3.6 Electron Shelving

Electron Shelving is a fluorescence-based state detection technique that allows us to determine the internal state of the ion with efficiency close to $\sim 100\%$. In this method, we use a metastable state (in our case, the $D_{5/2}$ state) as a "shelved" state, and the $S_{1/2} \leftrightarrow P_{1/2}$ as the "fast" transition for fluorescence detection. If the ion is in the $S_{1/2}$ state, it will scatter photons when illuminated

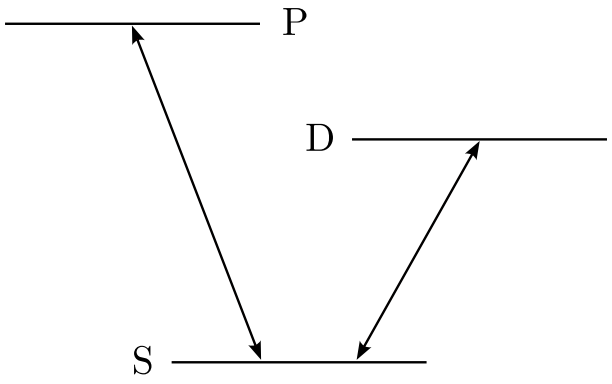

Figure 3.9: Schematic of the electron shelving technique for state detection. 397 nm and 866 nm light is shined on the ion, which causes fluorescence if the ion is in the $S_{1/2}$ state (bright state) and no fluorescence if the ion is in the $D_{5/2}$ state (dark state).

with the 397 nm and 866 nm lasers, resulting in a bright signal on the EMCCD camera. If the ion is in the $D_{5/2}$ state, it will not scatter photons (since it's not part of the cooling/detection cycle), resulting in a dark signal on the camera. This is very powerful for state detection since the $D_{5/2}$ state has a long lifetime of ≈ 1.2 seconds, which is our only theoretical limitation. This process can be repeated multiple times to find the coefficients of the state in the $S_{1/2}$ and $D_{5/2}$ basis.

3.3.7 Quantum Jumps

Quantum jumps refers to the rapid blinking of ion when the 729 nm beam is shined. The basic idea is that when the 729 nm beam is on continuously rather than pulsed, it can drive the ion from the bright $S_{1/2}$ state to the dark $D_{5/2}$ state with some probability. But, since the detection lasers are still on, they act as projection operators and the wavefunction of the ion collapses ("jumps") to one of the two states. If it collapses to the bright $S_{1/2}$ state, it will continue to fluoresce until the 729 nm beam drives it to the dark $D_{5/2}$ state again, causing another jump. This results in a random blinking pattern of the fluorescence signal, which can be observed on the EMCCD camera. For a detailed discussion on the fundamental nature of quantum jumps, refer Wineland, D. J. *et al* [33]. The time evolution of single ion fluorescence during jumps is shown in fig. 3.11 and EMCCD images of multi-ion jumps are shown in fig. 3.10.

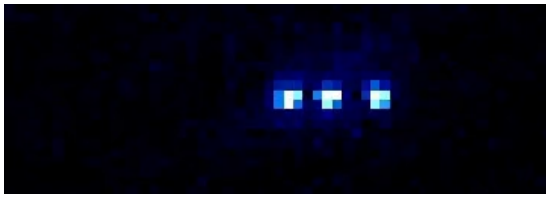

(a) State 1

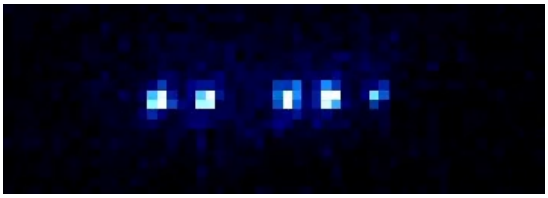

(b) State 2

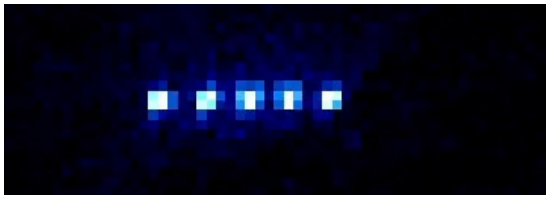

(c) State 3

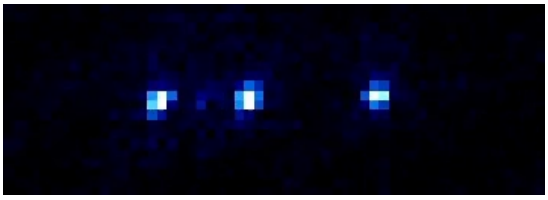

(d) State 4

Figure 3.10: Frames captured from the EMCCD camera that are 500 ms apart, showing the quantum jumps of the 6 ions between the bright and dark states.

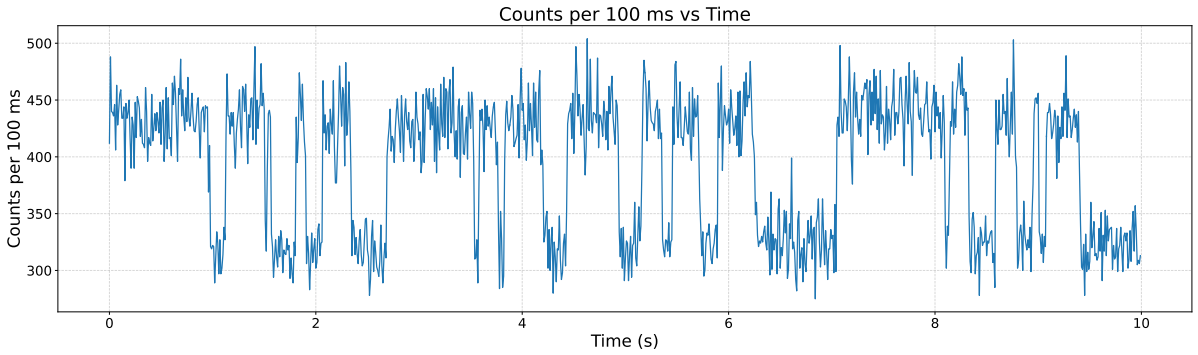

Figure 3.11: The photon count rate of a single ion is recorded using a PMT for 10 seconds while the 729 nm laser is shined on it. The high and low count states represent the bright and dark states of the ion.

We aligned the beam for optimal overlap with the ions by using the camera at large (~ 0.1s) exposure times, so that what we observe, is an average drop in the fluorescence of the ion. This is because the rate of quantum jumps is much higher than the shutter speed. The frequency of the 854 nm beam can also be optimized by trying to cancel the drop in fluorescence by detuning the beam at low power, which happens when the 854 nm beam efficiently repumps the population from the $D_{5/2}$ state back to the cooling cycle and thus, fluoresces. Our operating frequency for the 854 nm repumper is $\approx$ 350.86295 THz. This is a crucial step for state reinitialization after each experiment run, and also a possible cause of decoherence if not optimized properly.

Chapter 4

Results

4.1 Trapping and Imaging Ions

Ions are initially loaded (photoionization beams kept on for $>$ 5 mins at least) in large numbers as ion "clouds" (as shown in fig. 4.1) for easy detection. This is done at low RF and DC voltages to create a wide and shallow potential well, to trap more ions.

Figure 4.1: Fluorescence image of a large ion cloud containing hundreds of ions, captured by the EMCCD camera.

We reposition the 397 nm beam and use the EMCCD camera to track and find the position of the ion cloud. All this while, the 866 nm is toggled on and off to distinguish the ion fluorescence from background scatter. Once located, we try to maximize the fluorescence signal by optimizing the beam alignment, frequency and focus of the objective/camera.

We further blue detune the cooling lasers to condense the ion cloud to form Coulomb crystals and linear strings of ions (as shown in fig. 4.2). By restricting the loading time to a few seconds, we can load single ions.

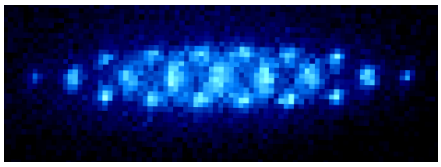

(a) Coloumb crystal

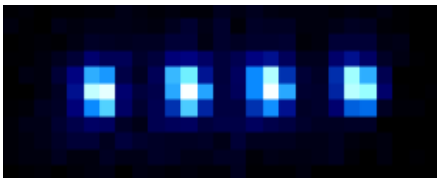

(b) Linear string of 4 ions

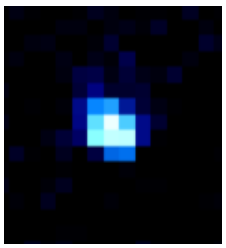

(c) Single ion

Figure 4.2: Fluorescence images of ion crystals formed under different conditions.

4.2 Spectroscopy on the Quadrupole Transition

Spectroscopy of the qubit transition is done in a pulsed sequence as shown in fig. 4.3.

	Step #	Duration (us)	AOM 397_Doppler	AOM 866	AOM 397_Pumping	AOM 854	AOM 729_Addressing	TTL Camera
1	1	4000	ON	ON	OFF	ON	OFF	OFF
2	2	50	OFF	ON	ON	OFF	OFF	OFF
3	3	100	OFF	OFF	OFF	OFF	ON	OFF
4	4	10000	ON	ON	OFF	OFF	OFF	ON

Figure 4.3: Pulsed sequence used for spectroscopy of the $S_{1/2} \leftrightarrow D_{5/2}$ quadrupole transition.

Spectroscopy is done in the following steps:

1. Doppler cooling for 4 ms to cool the ion close to the Doppler limit.
2. Optical pumping for 50 μs to prepare the ion in the $S_{1/2}(m_j = 1/2)$ state.

3. A pulse of the 729 nm beam with a certain duration and frequency is applied to drive the ion to the $D_{5/2}$ state with some probability.

4. State detection is done by electron shelving (see section 3.3.6) where the 397 nm and 866 nm beams are turned on for 10 ms and the image is captured by the camera triggered on this step.

5. The sequence is repeated multiple times (typically 100) for the same pulse duration and frequency to get a good estimate of the population transfer probability.

6. The 729 AOM frequency is incremented after every 100 iterations and this is repeated until the desired frequency range is covered.

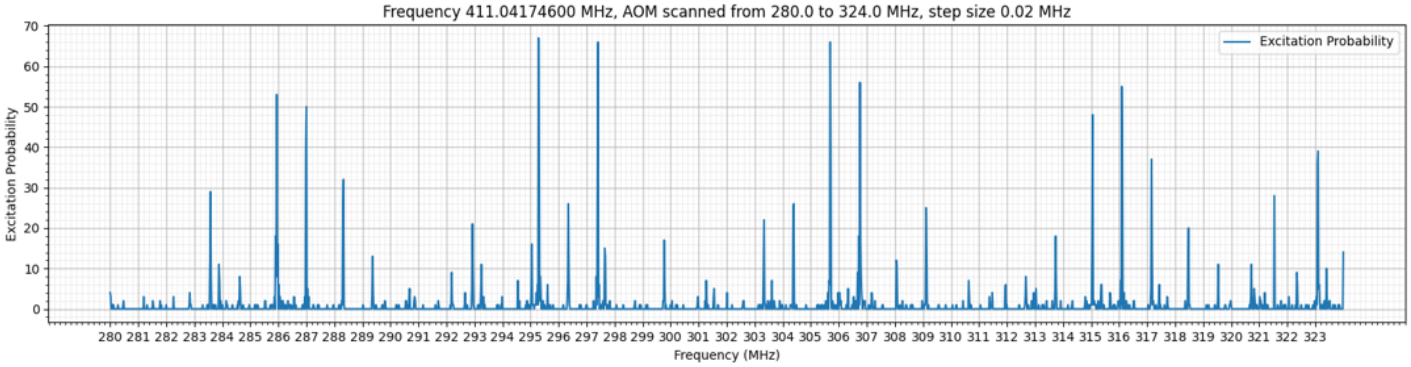

Figure 4.4: Spectrum of the qubit transition obtained by plotting the population transfer probability (out of 100) as a function of frequency shift to the laser post double-pass.

All our pulse sequences are triggered on the zero crossing of main AC line. This is done because fluctuations in the AC line can affect the $\vec{B}$ field which in turn affects the transition frequency, resulting in a broadening of the spectrum. By triggering on the zero crossing, we ensure that the $\vec{B}$ field is at a constant point in its cycle for each run of the experiment. However, this also limits our repetition rate to 50 Hz (20 ms), which is a bottleneck for data collection. Active field stabilization is a possible solution to this problem, which we plan to implement in the future.

Optical pumping

Optical pumping is done to prepare the ion in a specific Zeeman sublevel of the $S_{1/2}$ state, if not which the population would be distributed between the two sublevels, which would lead to a reduction in the maximum population transfer probability to the $D_{5/2}$ state. The optical pumping beam is σ^+ polarized and is resonant (in contrast with the doppler beam, which is red

detuned) with the $S_{1/2}(m_j = -1/2) \leftrightarrow P_{1/2}(m_j = 1/2)$ transition, which optically pumps the population to the $S_{1/2}(m_j = 1/2)$ state.

The polarization is set using a quarter waveplate and spatial overlap is optimized by maximizing ion fluorescence when the optical pumping beam is sent through the same fiber as the 422 nm beam along the $\vec{B}$ turned on. Since this is on resonance with the cooling transition, we need to keep the power low (a few μW) and the duration short (tens of μs) to avoid heating up of the ion. The efficiency is improved by either suppressing or maximizing one of the peaks in the spectrum by rotating the quarter waveplate. Thus, we will have two positions on the waveplate (corresponding to transitions from $S_{1/2}(m_j = 1/2)$ and $S_{1/2}(m_j = -1/2)$) where one set of peaks is suppressed and another set enhanced.

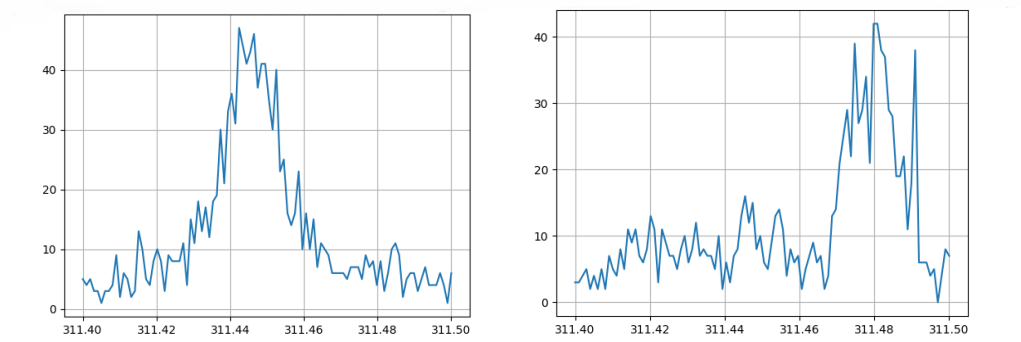

(a) Waveplate position 1 (b) Waveplate position 2 (90° rotation from position 1)

Figure 4.5: Optical pumping of the $S_{1/2}$ state using a quarter waveplate.

Clearly we see (in fig. 4.5) that one peak is suppressed and another is enhanced at the two positions, which correspond to the ion being pumped to either of the two Zeeman sublevels.

State detection

As discussed in section 3.3.6, the state of the ion is detected by turning on the cooling and repumper beams and capturing the fluorescence image with the EMCCD camera. A histogram of the summed total counts from each pixel in a frame for 100 frames, can be used to set a threshold for state discrimination. Anything below the threshold is classified as the ion being in the dark $D_{5/2}$ state and anything above is classified as the bright $S_{1/2}$ state. A good threshold would be one that minimizes the overlap between the two distributions to reduce misclassification errors. Each point in the spectrum (see fig. 4.4) is obtained by counting the number of frames (out of 100) that are classified as dark (below set threshold), which gives us the population transfer probability to the $D_{5/2}$ state.

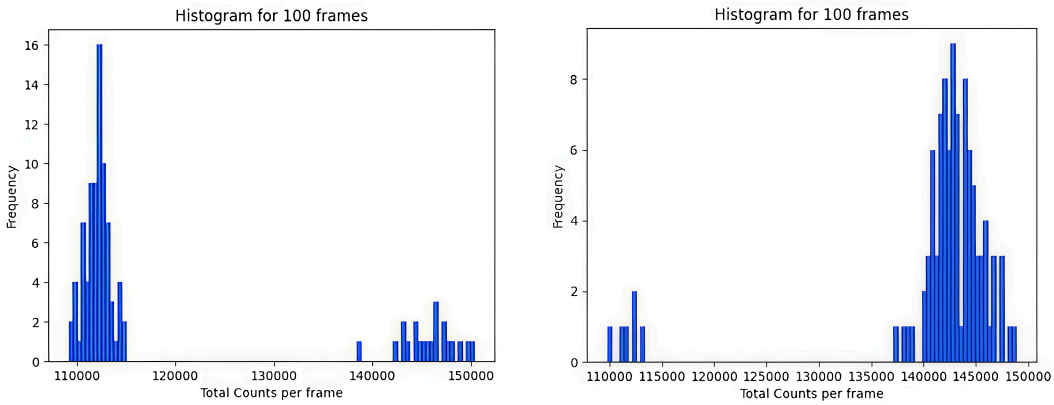

(a) Dark State ($D_{5/2}$)

(b) Bright State ($S_{1/2}$)

Figure 4.6: State detection histograms for the dark and bright states. A good threshold here would be around 125000.

4.3 Characterization of the Spectrum

This section is dedicated to the characterization of the spectrum obtained in fig. 4.4. We identify each of the peaks in the spectrum as carrier, secular sidebands and micromotional sidebands. This is done by varying parameters such as the RF voltages and $\vec{B}$ field.

4.3.1 RF Analysis

A spectrum is taken at three different RF voltages by varying the attenuator voltage (see section 3.1.1) in equal steps. Note that this doesn't guarantee a linear change in the RF voltage (since the attenuator works in a logarithmic scale), but we can back calculate the RF voltage from the measured secular frequencies. The idea is that, carrier transition should not change with the RF voltage, while the radial sidebands should shift away from the carriers with increase in RF voltage (refer eq. (2.18)).

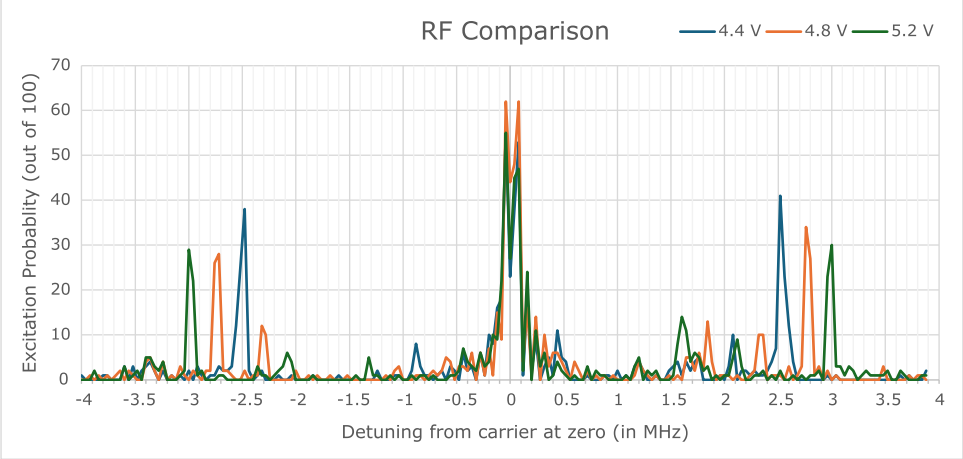

Figure 4.7: RF analysis of the spectrum. The carrier peak (at zero) remain unchanged while the radial sidebands (in blue, orange and green) shift away from the carrier with increase in RF voltage.

In fig. 4.7 the peak blue detuned from the carrier is the blue radial sideband and the peak red detuned from the carrier is the red radial sideband. The radial secular frequencies are measured to be between 2.5 MHz and 3 MHz for the range of RF attenuator voltages used.

The axial sidebands are not visible in this spectrum since we are addressing the ion along the radial direction and thus have very little projection of the 729 nm $\vec{k}$ (refer eq. (2.39)) along the axial direction, which results in a very small coupling strength to the axial modes. Yet, we have seen axial sidebands with a small excitation in finer scans around the carrier as shown in fig. 4.8.

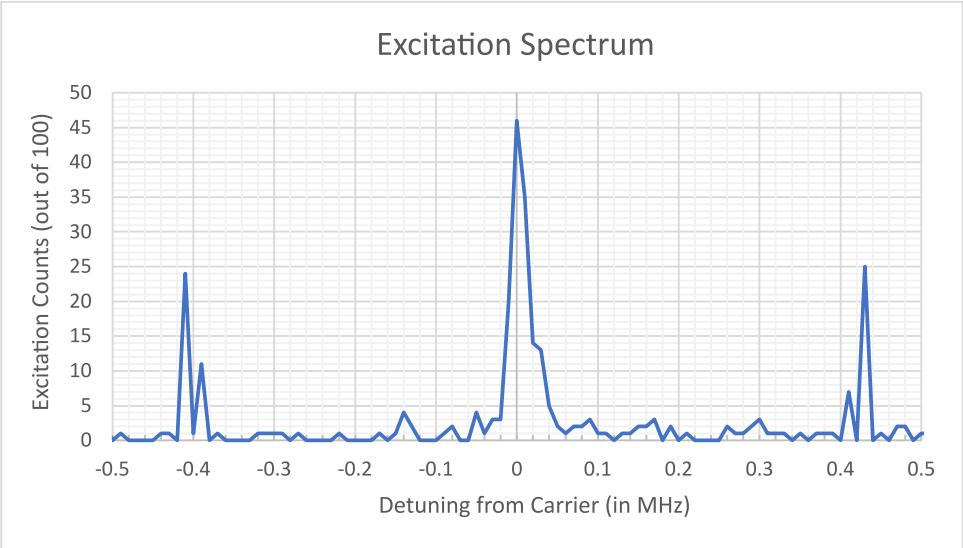

Figure 4.8: Axial sidebands around a carrier for a $V_{\mathrm{DC}} \sim 400$ V.

Carrier (MHz)	Voltage (V)	Blue Side (MHz)	Red Side (MHz)	Δ Blue (MHz)	Δ Red (MHz)
274.96	5.2	278	272	3.04	2.96
274.96	4.8	277.76	272.24	2.8	2.72
274.96	4.4	277.48	272.48	2.52	2.48
285.12	5.2	288.12	282.12	3	3
285.12	4.8	287.88	282.4	2.76	2.72
285.12	4.4	287.64	282.64	2.52	2.48
294.76	5.2	297.76	291.84	3	2.92
294.76	4.8	297.52	292.04	2.76	2.72
294.76	4.4	297.28	292.24	2.52	2.52
304.92	5.2	307.88	301.96	2.96	2.96
304.92	4.8	307.64	302.16	2.72	2.76
304.92	4.4	307.44	302.36	2.52	2.56
309.52	5.2	312.44	306.56	2.92	2.96
309.52	4.8	312.24	306.76	2.72	2.76
309.52	4.4	312	306.96	2.48	2.56
314.56	5.2	317.52	311.64	2.96	2.92
314.56	4.8	317.28	311.8	2.72	2.76
314.56	4.4	317.08	312	2.52	2.56
324.68	5.2	327.64	321.76	2.96	2.92
324.68	4.8	327.44	321.96	2.76	2.72
324.68	4.4	327.2	322.16	2.52	2.52

Table 4.1: Potential Carrier and their radial secular frequencies extracted from fig. 4.9

We do a similar analysis for the entire frequency range as shown in fig. 4.9 and identify the peaks as tabulated in table 4.1.

One loophole in this line of thought is that even micromotional sidebands remain unshifted with change in RF voltage, although there could be a change in amplitude. Thus we find more than five (the expected number of carriers after optical pumping, see fig. 2.8b) peaks that remain unchanged with change in RF voltage, which could be a result of micromotional sidebands. To confirm this, we do a $\vec{B}$ field analysis.

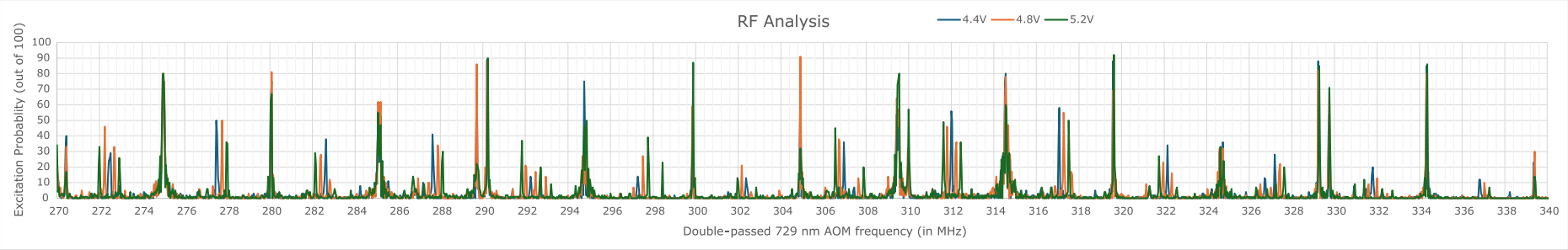

Figure 4.9: RF analysis of the spectrum. The carrier peaks remain unchanged while the radial sidebands (in blue, orange and green) shift away from the carrier with increase in RF voltage.

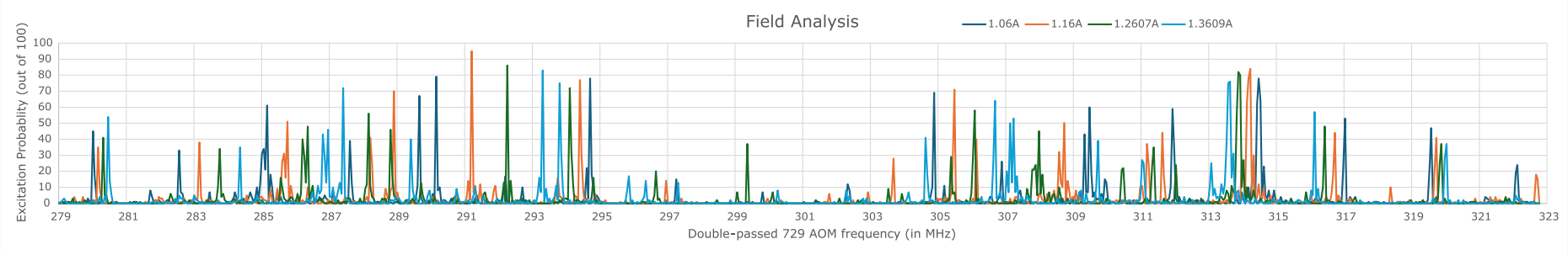

Figure 4.10: $\vec{B}$ field analysis of the spectrum. The carrier peaks shift away from the zero field point (refer section 3.2.2) with increase in field coil current.

4.3.2 $\vec{B}$ Field Analysis

From eq. (2.30) it can be derived that:

$$m_j \rightarrow m_{j'} = A + m_{j'}\Delta E_D - m_j \Delta E_S \tag{4.1}$$

where A is the zero field separation as in fig. 2.8b, ΔE_D is the Zeeman splitting of the $D_{5/2}$ state and ΔE_S is the Zeeman splitting of the $S_{1/2}$ state.

It can be inferred from the above equation that, a carrier peak corresponding to a transition from $S_{1/2}(m_j)$ to $D_{5/2}(m_{j'})$, always shifts away linearly from the zero field point (A) with increase in $\vec{B}$ field. Thus, any carrier (and its associated sidebands) at the left of the zero field point shifts to the left with increase in $\vec{B}$ field, and any carrier (and its associated sidebands) at the right of the zero field point shifts to the right with increase in $\vec{B}$ field.

4.3.3 Identification of carrier peaks

From fig. 4.10 we can see that some of the unchanged peaks in fig. 4.9 shift in the opposite direction with an increase in $\vec{B}$ field, from what is expected from a carrier transition. This suggests that they could be micromotional sidebands belonging to a carrier on the other side of the spectrum. These sidebands will be at ± 19.77 MHz (the RF drive frequency) from the carrier peaks, thus we go to a much lower field (from 1.26 A to 0.4 A) to avoid overlap of the micromotional sidebands with the carrier peaks, which makes the analysis difficult.

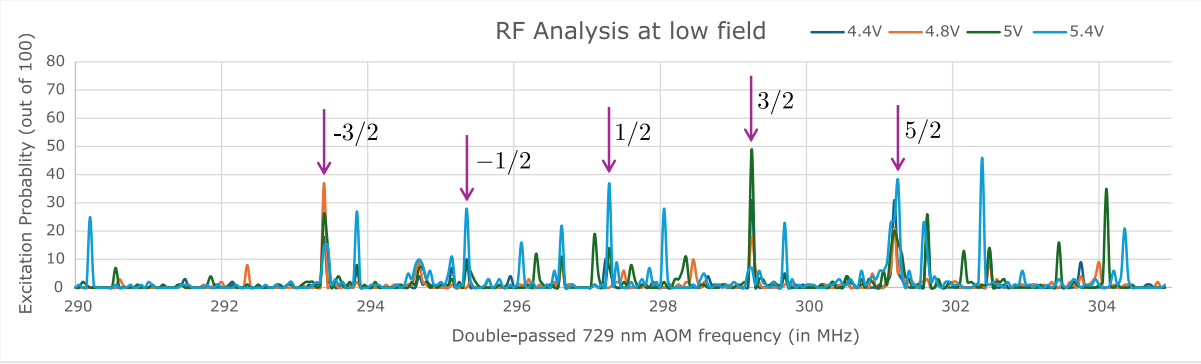

Figure 4.11: $\vec{B}$ field analysis of the spectrum at low field.

From table 4.2 the inter-carrier separation is around 1.95 MHz. We need to maintain a separation of at least 6.5 MHz between carriers to avoid overlap of radial sidebands of one carrier with the carrier peak of another. Thus, we need to work at higher fields. We increase

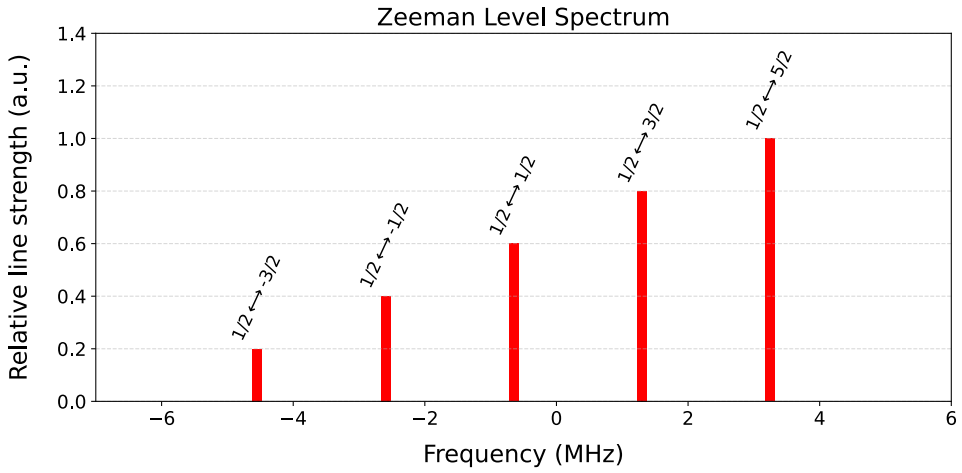

(a) Calculated spectrum at 1.95 MHz inter-carrier separation

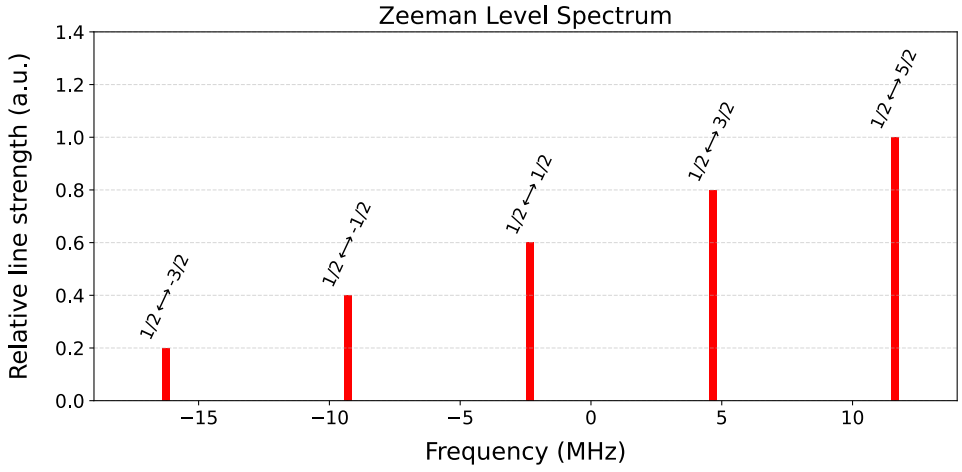

(b) Calculated spectrum at 6.97 MHz inter-carrier separation

Figure 4.12: Comparison of calculated Zeeman spectra for different inter-carrier separations.

Transition	Frequency (MHz)
$D_{5/2}(-3/2)$	293.45
$D_{5/2}(-1/2)$	295.4
$D_{5/2}(1/2)$	297.35
$D_{5/2}(3/2)$	299.3
$D_{5/2}(5/2)$	301.25

Table 4.2: Carrier transition frequencies for the $S_{1/2}(m_j = 1/2) \rightarrow D_{5/2}(m_{j'})$ transitions at 0.4 A

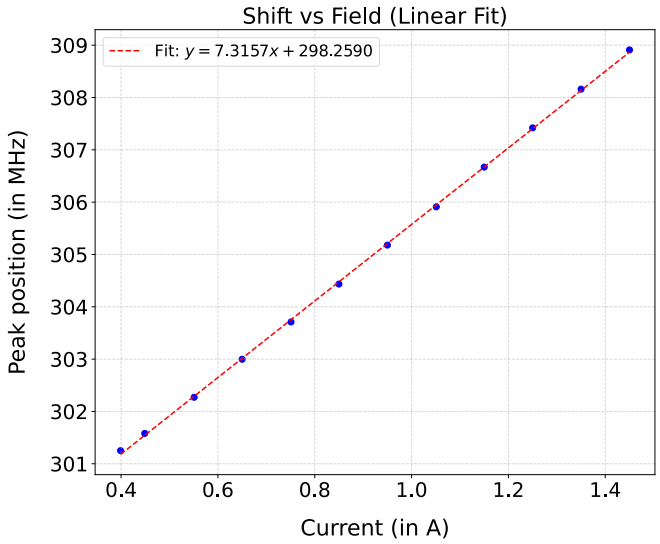

Figure 4.13: Shift of the $1/2 \rightarrow 5/2$ transition with increasing $\vec{B}$ field.

the field current in a step-wise manner and track the $1/2 \rightarrow 5/2$ transition (the rightmost peak) to find a field where the inter-carrier separation is around 6.97 MHz (corresponding to a field of around 4.15 G), which is achieved when the $1/2 \rightarrow 5/2$ transition shifts by $11.61 - 3.24 = 8.37$ MHz (refer fig. 4.12).

We can see from fig. 4.13 that the shift is linear with field, which is expected from eq. (4.1). From the characterization of the shift, we calculate that the current required for our desired shift is 1.55 A. Thus, this is our operating field current with a field of 4.15 G at the ions.

All identified carrier peaks at this field along with their frequencies and the corresponding peak plots are shown in table 4.3.

Transition	Frequency (MHz)	Carrier Peak Plot
$D_{5/2}(-3/2)$	281.68	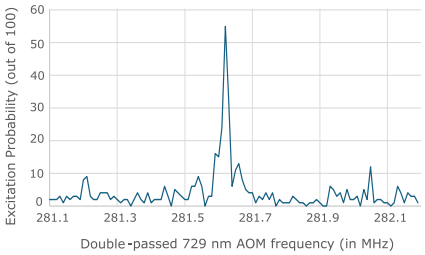
$D_{5/2}(-1/2)$	288.69	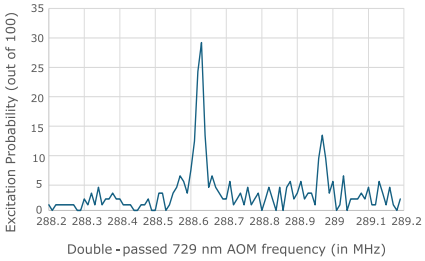
$D_{5/2}(1/2)$	295.66	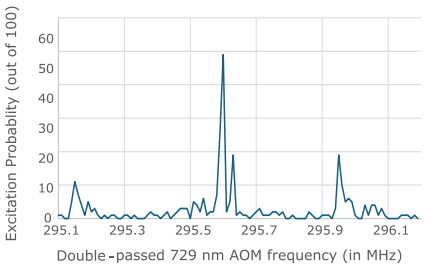
$D_{5/2}(3/2)$	302.63	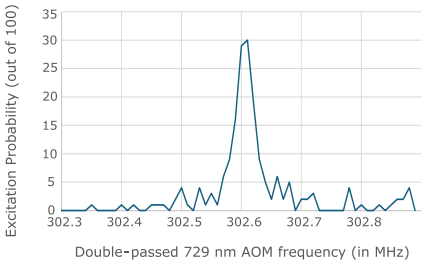
$D_{5/2}(5/2)$	309.6	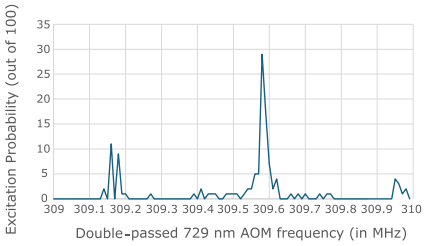

Table 4.3: Carrier transition frequencies for the $S_{1/2}(m_j = 1/2) \rightarrow D_{5/2}(m_{j'})$ transitions at 1.55 A

4.4 Observation of Rabi Oscillations

Rabi oscillations are observed by varying the **duration** of the 729 nm pulse at Step 6 and fixing the frequency (in contrast to the varying the frequency at a fixed duration) in the pulsed sequence described in section 4.2 and plotting the population transfer probability as a function of the pulse duration.

4.4.1 Pulse Time vs. Population Transfer

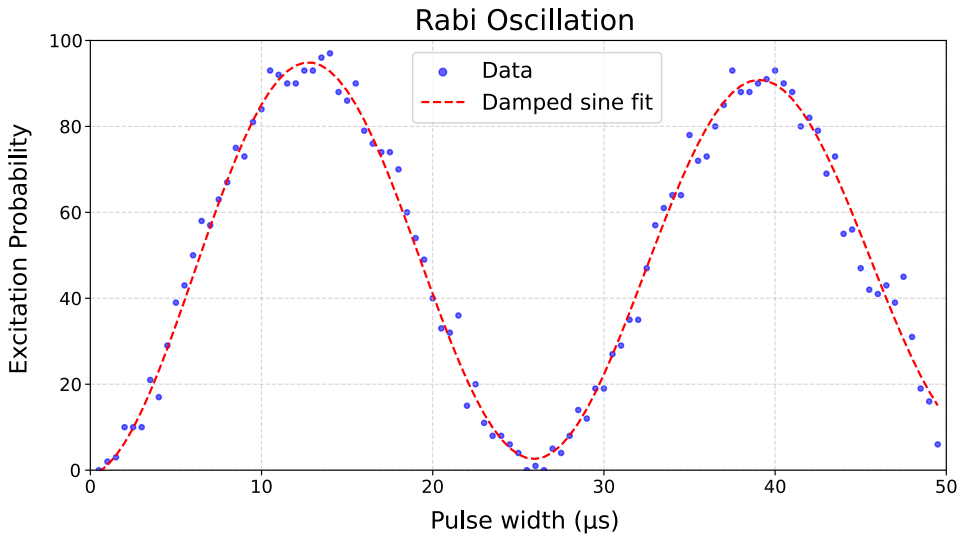

Figure 4.14: Rabi oscillation data fitted with a damped sine wave.

Rabi oscillations obtained on the $1/2 \rightarrow 1/2$ transition at 295.66 MHz are shown in fig. 4.14. A damped sine wave is fitted to the data to estimate the Rabi frequency and π-time. The fitted Rabi frequency is $\Omega = 2\pi \times 37.98$ KHz and a π-time of $t_\pi = 13.17\mu$s is obtained from the fit.

4.4.2 Probe time Analysis

The Rabi frequency can also be extracted from the frequency spectrum obtained by fitting eq. (2.26) as a function of the detuning Δ at a known probe time t.

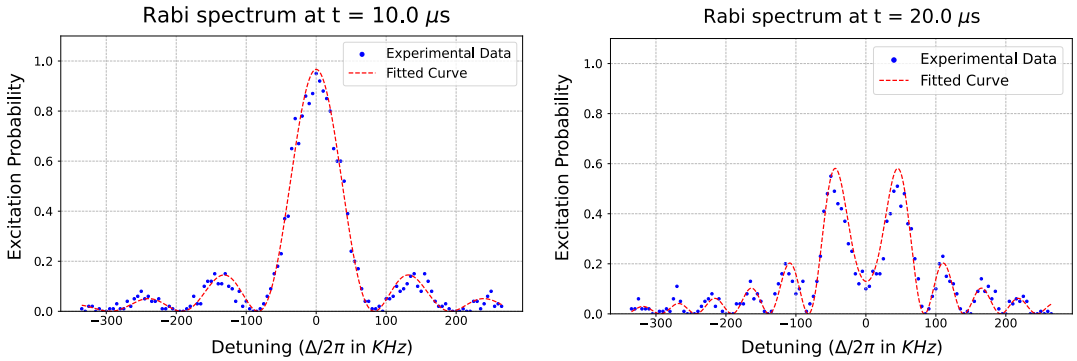

(a) t = 10 μs

(b) t = 20 μs

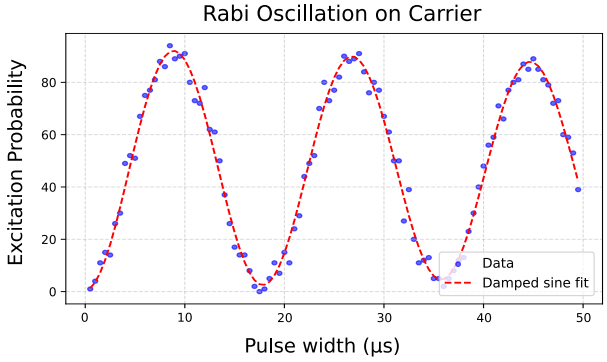

(c) Rabi at peak of the spectrum

Figure 4.15: (a) and (b) Frequency spectrum of the $1/2 \rightarrow 1/2$ transition for two different probe times. (c) Rabi oscillation at the corresponding zero detuning point.

The Rabi frequency from the frequency spectrum fit is $\Omega_{spectrum} = 2\pi \times 54.22$ KHz, which is close to the value obtained from the Rabi oscillation fit of $\Omega_{rabi} = 2\pi \times 55.81$ KHz.

4.4.3 Doppler Cooling Efficiency

The difference in the Rabi frequencies obtained from the two methods can be attributed to the low coherence time of the system, due to the presence of multiple carrier transitions at the same 729 nm frequency (but different Rabi frequencies, see eq. (2.43)) for different phonon numbers, which leads to a faster decay of the Rabi oscillations and a higher fitted Rabi frequency [34]. This is ultimately due to heating up of the ion (which could be a consequence of inefficient cooling), consequently a higher mean phonon number and a broader distribution of phonon numbers in the thermal state of the ion.

$$|c_2(t)|^2 = \sum_{n=0}^{\infty} P_n(\bar{n}) \sin^2\left(\frac{\Omega_{n,n}}{2}t\right) \tag{4.2}$$

$P_n(\bar{n})$ is the thermal phonon distribution for a mean phonon number $\bar{n}$.

$$P_n(\bar{n}) = \frac{1}{\bar{n}+1}\left(\frac{\bar{n}}{\bar{n}+1}\right)^n \tag{4.3}$$

Thus, fitting the Rabi oscillation data with such a model that takes into account the thermal phonon distribution, can provide an estimate of the mean phonon number $\bar{n}$ and the Rabi frequency at $n = 0$ (which is the ideal Rabi frequency in the absence of heating).

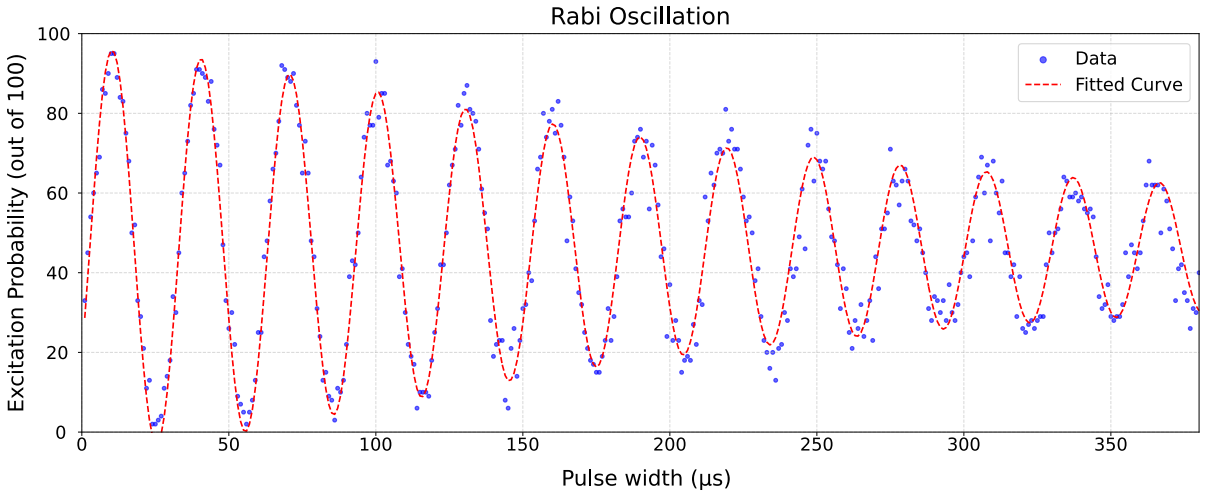

Figure 4.16: Rabi oscillation data fitted with eq. (4.2) and $\bar{n}$, Ω_0 as fit parameters.

By fitting the rabi data with the model in eq. (4.2), we obtain a mean phonon number of $\bar{n} = 9.562 \pm 0.248$ and a Rabi frequency at $n = 0$ of $\Omega_0 = 2\pi \times 34.14 \pm 0.02$ KHz.

4.5 Calculation of Trap parameters

$$\alpha = \frac{2\omega_z^2 L^2}{(q/m)_{\mathrm{Ca}^+} \cdot V_{\mathrm{DC}}} = 0.39 \pm 0.02 \tag{4.4}$$

$$\mathrm{q} = \sqrt{\left(\omega_r^2 + \frac{\omega_z^2}{2}\right)\frac{8}{\Omega_{\mathrm{RF}}^2}} = 0.34 \pm 0.001 \tag{4.5}$$

$$V_{\mathrm{RF}} = \frac{\mathrm{q}(\Omega_{\mathrm{RF}} r_0)^2}{2\,(q/m)_{\mathrm{Ca}^+}} = 707\ \mathrm{V} \pm 18\mathrm{V} \tag{4.6}$$

$$\eta = k\sqrt{\frac{\hbar}{2(40 \cdot m_u)\omega_r}} = 0.062 \pm 0.001 \tag{4.7}$$

Errors are estimated by propagation in quadrature:

$$\delta f = \sqrt{\sum_i \left(\frac{\partial f}{\partial x_i} \delta x_i \right)^2} \tag{4.8}$$

All the parameters are calculated using the measured secular frequencies ω_z (400 KHz) and ω_r (2.4 MHz) and the known values of L (5.86 mm), r_0 (0.8 mm), Ω_{RF} (19.77 MHz) and V_{DC} (460 V). The errors are calculated assuming 0.01 mm machining tolerance, 10 KHz resolution of frequency spectrum and 1 KHz drift in RF resonance.

The calculated value of the stability parameter q is 0.34, which is within the stable trapping range as described in section 2.2.3.

The Lamb-Dicke parameter η is calculated to be approximately 0.06, thus $\eta^2(2\bar{n}+1) \approx 0.07 \ll 1$, which confirms that we are in the Lamb-Dicke regime.

Chapter 5

Conclusion and Future Outlook

This chapter summarizes the key findings of this thesis and discusses their implications for the field of quantum information processing. We also outline potential future research directions, including the implementation of multi-qubit gates.

5.1 Summary of Key Findings

The goal of this thesis was to demonstrate a physical system for quantum information processing using trapped ions satisfying the DiVincenzo criteria. In this thesis, we:

- Single and multiple $^{40}Ca^{+}$ ions successfully trapped and imaged in a linear Paul trap.
- Characterized the spectrum of the qubit transition and identified the carrier and motional sidebands.
- Implemented Doppler cooling to reduce the motional energy of the ions, achieving near-ground-state cooling ($\bar{n} \approx 9.5$).
- Demonstrated rabi oscillations, showing coherent control over the internal states of the ions over good coherence times.

5.2 Future Outlook: Towards Entanglement and Two-Qubit Gates

The next steps in our research will focus on implementing multi-qubit gates and generating entanglement between ions. This will involve three main directions:

- **Sideband Cooling:** We will implement sideband cooling to initialize the qubit in the motional ground state which is essential for improving coherence times as well as for two-qubit protocols such as Cirac-Zoller gates.
- **Single-ion addressing:** We will implement single-ion addressing using tightly focused laser beams and crossed AODs which is essential for implementing multi-qubit gates and generating entanglement.
- **Active stabilization:** We will implement active stabilization of the magnetic field and RF fields to mitigate decoherence due to field fluctuations by taking feedback from the qubit spectrum.

Bibliography

[1] Max Tegmark and John Archibald Wheeler. 100 years of quantum mysteries. *Scientific American*, 284(2):68–75, 2001.

[2] Richard P. Feynman. Simulating physics with computers. *International Journal of Theoretical Physics*, 21(6/7):467–488, 1982.

[3] Peter W. Shor. Polynomial-time algorithms for prime factorization and discrete logarithms on a quantum computer. *SIAM Journal on Computing*, 26(5):1484–1509, October 1997.

[4] Lov K. Grover. A fast quantum mechanical algorithm for database search, 1996.

[5] David P. DiVincenzo. The physical implementation of quantum computation. *Fortschritte der Physik*, 48(9–11):771–783, 2000.

[6] National Science Review. Advancements in superconducting quantum computing. *National Science Review*, 12(8), 2025.

[7] PsiQuantum. Fault-tolerant architecture for photonic quantum computing. Technical report, PsiQuantum, 2024.

[8] Raoul Heese, Martin Gerke, Priska Steiner, Duarte Magano, Manuel Brouard, Julian Grabarczyk, David Mauch, Philine Schiewe, and Sven Jäger. Neutral atom quantum computing hardware: performance and end-user perspective. *EPJ Quantum Technology*, 10(1):32, 2023. arXiv:2304.14360.

[9] Guido Burkard, Thaddeus D. Ladd, Andrew Pan, John M. Nichol, and Jason R. Petta. Semiconductor spin qubits. *Rev. Mod. Phys.*, 95:025003, Jun 2023.

[10] IonQ. Benchmarking a trapped-ion quantum computer with 30-36 algorithmic qubits (AQ36). *Quantum Journal*, 2024.

[11] S. A. Moses et al. A race-track trapped-ion quantum processor. *Phys. Rev. X*, 13:041052, Dec 2023.

[12] F.M. Penning. Die glimmentladung bei niedrigem druck zwischen koaxialen zylindern in einem axialen magnetfeld. *Physica*, 3(9):873–894, 1936.

[13] Wolfgang Paul and Helmut Steinwedel. Ein neues massenspektrometer ohne magnetfeld. *Zeitschrift für Naturforschung A*, 8(7):448–450, 1953.

[14] E. Fischer. Three-dimensional stabilization of charged particles in a quadrupole field. *Zeitschrift für Physik*, 156(1):1–26, 1959.

[15] R. F. Wuerker, H. Shelton, and R. V. Langmuir. Electrodynamic containment of charged particles. *Journal of Applied Physics*, 30(3):342–349, 1959.

[16] David J. Wineland, James C. Bergquist, John J. Bollinger, and Wayne M. Itano. *Trapped Ions and Laser Cooling: Selected Publications of the Ion Storage Group of the Time and Frequency Division, NBS, Boulder, Colorado*. NIST Special Publication 778. National Institute of Standards and Technology (NIST), 1990.

[17] W. Neuhauser, M. Hohenstatt, P. E. Toschek, and H. Dehmelt. Localized visible Ba^+ mono-ion oscillator. *Physical Review A*, 22(3):1137–1140, 1980.

[18] J. I. Cirac and P. Zoller. Quantum computations with cold trapped ions. *Phys. Rev. Lett.*, 74:4091–4094, May 1995.

[19] David P. DiVincenzo. Two-bit gates are universal for quantum computation. *Physical Review A*, 51(2):1015–1022, 1995. arXiv:cond-mat/9407022.

[20] F. Schmidt-Kaler, H. Häffner, S. Gulde, M. Riebe, G.P.T. Lancaster, T. Deuschle, C. Becher, W. Hänsel, J. Eschner, C.F. Roos, and R. Blatt. How to realize a universal quantum gate with trapped ions. *Applied Physics B*, 77(8):789–796, December 2003.

[21] C. Monroe, D. M. Meekhof, B. E. King, W. M. Itano, and D. J. Wineland. Demonstration of a fundamental quantum logic gate. *Physical Review Letters*, 75(25):4714–4717, 1995.

[22] Michael A. Nielsen and Isaac L. Chuang. *Quantum Computation and Quantum Information*. Cambridge University Press, Cambridge, 10th anniversary edition, 2010.

[23] Brian C. Hall. An elementary introduction to groups and representations. *arXiv preprint math-ph/0005032*, pages 36, 51, 2000.

[24] Pradip K. Ghosh. *Ion Traps*. Number 90 in International Series of Monographs on Physics. Clarendon Press, Oxford, 1995.

[25] D. J. Berkeland, J. D. Miller, J. C. Bergquist, W. M. Itano, and D. J. Wineland. Minimization of ion micromotion in a Paul trap. *Journal of Applied Physics*, 83(10):5025–1033, 1998.

[26] Daniel F. V. James. Quantum computation with hot and cold ions: An assessment of proposed schemes. *Fortschritte der Physik*, 48(9–11):823–837, 2000.

[27] A. Kramida, Yu. Ralchenko, J. Reader, and and NIST ASD Team. NIST Atomic Spectra Database (ver. 5.12), [Online]. Available: `https://physics.nist.gov/asd` [2026, January 8]. National Institute of Standards and Technology, Gaithersburg, MD., 2024.

[28] J. Jin and D. A. Church. Precision lifetimes for the Ca^+ $4p\ ^2p$ levels: Experiment challenges theory at the 1% level. *Physical Review Letters*, 70(21):3213–3216, 1993.

[29] P. A. Barton, C. J. S. Donald, D. M. Lucas, D. A. Stevens, A. M. Steane, and D. N. Stacey. Measurement of the lifetime of the $3d\ ^2D_{5/2}$ state in $^{40}Ca^+$. *Physical Review A*, 62(3):032503, 2000.

[30] Daniel F. V. James. Quantum dynamics of cold trapped ions with application to quantum computation. *Applied Physics B*, 66(2):181–190, 1998.

[31] Christian F. Roos. *Controlling the quantum state of trapped ions*. PhD thesis, University of Innsbruck, 2000.

[32] Edwin T. Jaynes and Fred W. Cummings. Comparison of quantum and semiclassical radiation theories with application to the beam maser. *Proceedings of the IEEE*, 51(1):89–109, 1963.

[33] D. J. Wineland, J. C. Bergquist, J. J. Bollinger, W. M. Itano, C. Monroe, H. Seidelmann, D. M. Meekhof, B. E. King, D. Leibfried, and C. J. Myatt. Quantum effects in measurements on trapped ions. *Physica Scripta*, T59:286–292, 1995.

[34] Cornelius Hempel. *Digital quantum simulation, Schrödinger cat state spectroscopy and setting up a linear ion trap*. PhD thesis, University of Innsbruck, 2014.